Behavior of amagmatic orogenic geothermal systems: insights from the Agua Blanca Fault, Baja California, Mexico

Daniel Carbajal-Martínez [1, *], Christoph Wanner [1], Larryn W. Diamond [1], Loïc Peiffer [2, 3], John M. Fletcher [2], Claudio Inguaggiato [2] and Manuel Contreras-López [2]

[1] Rock–Water Interaction Group, Institute of Geological Sciences, University of Bern, Switzerland

[2] Departamento de Geología, Centro de Investigación Científica y de Educación Superior de Ensenada (CICESE), Ensenada, Baja California, México.

[3] Unidad La Paz (ULP), Centro de Investigación Científica y Educación Super bior de Ensenada (CICESE), La Paz, Baja California Sur, México.

Corresponding author: Daniel Carbajal-Martínez (carbadanmartinez@gmail.com)

Key points:

- Fault permeability and hydraulic head gradients control thermal–hydraulic behavior of amagmatic geothermal systems.
- The greater the fault permeability, the greater the magnitude of thermal anomalies.
- Temperature of amagmatic geothermal systems reaches the threshold for electricity production at shallow depth (< 4 km).

Abstract

Amagmatic geothermal systems within regional-scale orogenic faults are promising renewable resources for heat and possibly electricity production. However, their behavior needs to be better understood to improve exploration and assessment of their energy potential. To provide more insight, we report a geochemical, geological, and geophysical study of seven hot spring sites strung along a 90 km segment of the Agua Blanca Fault (ABF), which traverses a mountainous region of northern Baja California, Mexico. Our results show that topographic heads drive infiltration of meteoric water deep into basement rocks, where it is heated according to the local geothermal gradient (15–24 °C/km). Our diverse dataset provides strong evidence that the flow system, magnitude, and location of the thermal anomalies are primarily controlled by the permeability of the ABF system and the hydraulic head gradients. The hot water ascends along preferentially permeable zones, discharging at temperatures from 37 °C in inland springs to 102 °C at the Pacific coast. Higher temperatures correlate positively with the degree of extensional fault displacement

(a proxy for fault permeability). Correlations between hydraulic head gradients, residence times, and $^{3}He/He_{total}$ of the thermal waters show that the hydraulic head gradient controls the length and depth of the flow paths. Long paths to great depths lead to long water residence times and high $^{3}He/He_{total}$ fractions. Optimal conditions at the coast allow the 120 °C temperature threshold for electricity production to be reached at relatively shallow depths (< 4 km), demonstrating the potential of orogenic geothermal systems for petrothermal exploitation.

Plain Language Summary

The deep circulation of meteoric water in areas not affected by volcanoes represents underexplored renewable energy sources for heat or electricity production. A challenge for exploration is that the processes and forces that drive hot water circulation in such systems are not fully understood. To obtain new insights, we undertook a geochemical, geological, and geophysical study of seven hot spring sites strung along a 90 km long fault zone across the northern Baja California peninsula in Mexico. Our data show that rainwater infiltrates deep into mountainous areas and modifies its chemical composition and temperature, in the absence of any magmatic heat source. We also discovered that the local permeability of the fault zones controls the discharge temperature of the hot springs and, thus, the amount of thermal energy that could be potentially exploited from such systems. Other relevant system parameters, such as the depth of water infiltration and the subsurface water residence time, are controlled by the differences in water pressure under high and low points in the topography and by the distance between the point of infiltration of rainwater and its subsequent discharge location.

Keywords: Amagmatic orogenic geothermal system, Geothermal exploration, Fault permeability, Energy, Thermal water, Hydraulic head gradient

Abbreviations: Agua Blanca Fault (ABF), Brittle Ductile Transition Zone (BDTZ).

1 Introduction

Regional-scale faults in mountainous orogens often host hot springs with potential as geothermal resources, even in areas where magmatic heat is absent and heat fluxes are moderate, e.g., 60 mW m^{-2}. The springs are the discharge sites of meteoric water that have infiltrated at high altitudes, circulated deep into the fault plane where it acquired heat from the wall rocks, and then ascended through preferentially permeable upflow zones to low points in the topography (e.g., López & Smith, 1995; Alt-Epping et al., 2022)

Worldwide occurrences of such amagmatic orogenic geothermal systems include those in the Canadian Rocky Mountains (Grasby & Hutcheon, 2001), Lérida province in the Pyrenees in Spain (Asta et al., 2010), Da Qaidam in China (Stober et al., 2016), Brigerbad in Switzerland (Sonney & Vuataz, 2008), Eastern Pyrenees in France (Taillefer et al., 2018), Huangshadong in China (Tian et al., 2023), and along the Alpine Fault in New Zealand (Reyes et al., 2010). These fault-hosted, topography-driven systems are characterized by average crustal geothermal gradients of 20–30 °C km^{-1}, reservoir temperatures of 100–250 °C, and spring temperatures of 25–99 °C.

Recent studies have shown that the meteoric water in orogenic systems can penetrate to 10 km or more, allowing reservoir temperatures in amagmatic settings to attain significantly higher temperatures than previously expected (>250 °C; Diamond et al., 2018). Prolonged heat extraction from the wall rocks by water moving along the base of the circulation loop and its redeposition in the wall rocks of the upflow path can create large, three-dimensional, plume-like thermal anomalies beneath the discharge sites (Wanner et al., 2019). At depths within the reach of drilling (e.g., 2 km), the temperatures in these plumes can exceed the 120 °C threshold for electricity generation. Thus, although discharge rates are normally modest, the plumes of hot rock below the springs can be viewed as targets for petrothermal exploitation (Wanner et al., 2019).

To improve exploration strategies for this geothermal play, a better understanding is required of how they behave, particularly the controls on their locations and magnitudes. We have therefore undertaken a geochemical, geophysical, and geological study of orogenic geothermal systems along the Agua Blanca Fault (ABF) in Ensenada, NW Baja California, Mexico. We chose this topographically rugged area because it exhibits three favorable features: (1) seven geothermal systems are strung out along a ~90 km stretch of the fault, permitting quantitative correlation of hydraulic head gradients with the physicochemical properties of the springs; (2) water discharge temperatures vary along the fault from 37 to 102 °C (Vidal et al., 1981), the latter being worldwide

the hottest and therefore most prospective amagmatic system to our knowledge; (3) the host fault is active and the rates and magnitudes of tectonic extension along its segments have been quantified (Gold et al., 2020; Wetmore et al., 2019), allowing qualitative assessment of permeability variations along the fault.

In this paper, we take advantage of these features to explore how the interplay of variable fault permeability and hydraulic head gradients control the location and discharge temperatures of the springs. To enable this treatment, we present new analyses of spring compositions, including major solutes, pH, temperature, dissolved gases, O–H stable isotopes, and He–Ne radiogenic isotopes. We calculate water residence times and reservoir temperatures and interpret earthquake hypocenters to estimate depths to the brittle–ductile transition and geothermal gradients. Finally, we identify recharge zones from topographic maps, calculate hydraulic head gradients, and integrate our collective results with structural data from the literature. As well as providing new insight into the hydraulic controls on the geothermal systems, our new data and correlations will serve as calibration targets for future numerical simulations of water circulation through the Agua Blanca Fault, from which additional parameters can be quantified and conclusions drawn for exploration strategies.

1.1 Geology and geothermal manifestations of the study area

The study area lies in the northwest of the Baja California Peninsula, Mexico (Figure 1a), comprising the northwestern part of the Peninsular Ranges Batholith (PRB) geological province. Gastil et al. (1975) divided the rocks in the PRB into three tectonostratigraphic groups (Figure 1b): (i) Pre-batholithic rocks, consisting of a Triassic–Jurassic belt of metamorphosed quartz-bearing sandstone, argillite, and minor carbonate rocks located in the eastern part of the study area. Part of the same group is the Alisitos Formation, an Aptian–Albian belt of volcanic (andesite to dacite) and volcaniclastic (tuff and pyroclastic) rocks interbedded with sedimentary mudstone, sandstone, and limestone along the western flank of Baja California; (ii) Batholithic rocks of Cretaceous age dominated by tonalite (73 vol.%), granodiorite (23 vol.%), with minor gabbro and diorite (2 vol.%), and quartz monzonite (2 vol.%), which were emplaced successively from west to east between 140 and 80 Ma (U-Pb in zircon, Ortega-Rivera, 2003); (iii) Post-batholithic rocks comprising the Late Cretaceous Rosario Group of metavolcanic, granitic conglomerate, shale, and sandstone; Eocene–Paleocene marine sandstones and mudstones; and Miocene volcanic rocks (rhyolite, andesite, and basalt). The study area is dissected by three major, steeply dipping dextral

fault systems: Agua Blanca, Tres Hermanos, and San Miguel-Vallecitos. They host seventeen geothermal systems manifested by hot springs, submarine fumaroles, domestic thermal wells, and coastal thermal anomalies (Figure 1b, c).

The present study focuses on the geothermal systems along the active Agua Blanca Fault (ABF), a subvertical west–northwest-trending (276–302°) dextral–normal structure that first became active between 3.3 and 1.5 Ma (Wetmore et al., 2019). It is transtensional along its ~150 km exposed length and traverses nearly the entire Baja California Peninsula (Figure 1b), extending beneath the Pacific Ocean in the northwest. Although seismic events are infrequent and of low magnitude (>3 M_L, Ortega-Rivera et al., 2018), the ABF displays significant along-strike displacements of up to 12 km and slip rates of 3–4 mm/year (Wetmore et al., 2019; Gold et al., 2020). The surface trace of the ABF is marked by an abrupt topographic scarp along much of its length. The main fault has several branches, recognizable from geomorphological features such as triangular facets, deviated streams, vegetation lines, and uplifted marine terraces (Allen et al., 1960; Rockwell et al., 1989; Ortega-Rivera et al., 2018). Its trace rises from sea level eastward to over 1100 m a.s.l., passing through numerous topographic highs and lows, with an average elevation of 570 m a.s.l. (red line in Fig. 1d). The topography also rises towards the north of the fault trace to over 1500 m a.s.l., providing potential recharge areas for the fault. To illustrate this, a topographic profile parallel to and 3.5 km north of the fault is shown by the dotted line in Figure 1d, along which the average elevation is 920 m a.s.l.

Thermal waters are known to discharge in five valleys intersected by faults belonging to the ABF system. From east to west, these are Valle Trinidad, Cañon de Dolores, Valle Agua Blanca, Valle Santo Tomas, and Punta Banda (Figure 1d). The hottest thermal waters discharge on the coast of the Punta Banda Peninsula at La Jolla beach (LJB; Figure 1c) and in a submarine fumarolic field (SMF; Figure 1b). Their temperatures are 93 °C at 20 cm below the beach surface and 102 °C at 30 m b.s.l., respectively (Vidal et al., 1981; Carbajal-Martínez et al., 2020). Chemical and isotopic analyses of water and gas discharges in the study area have established their meteoric origin and have revealed no evidence of a magmatic heat source, in accord with the absence of any post-Miocene magmatic rocks (Vidal et al., 1981; Gastil & Bertine, 1986; Polyak et al., 1991; Beltrán-Abaunza & Quintanilla-Montoya, 2001; Arango-Galván et al., 2011; Barry et al., 2020).

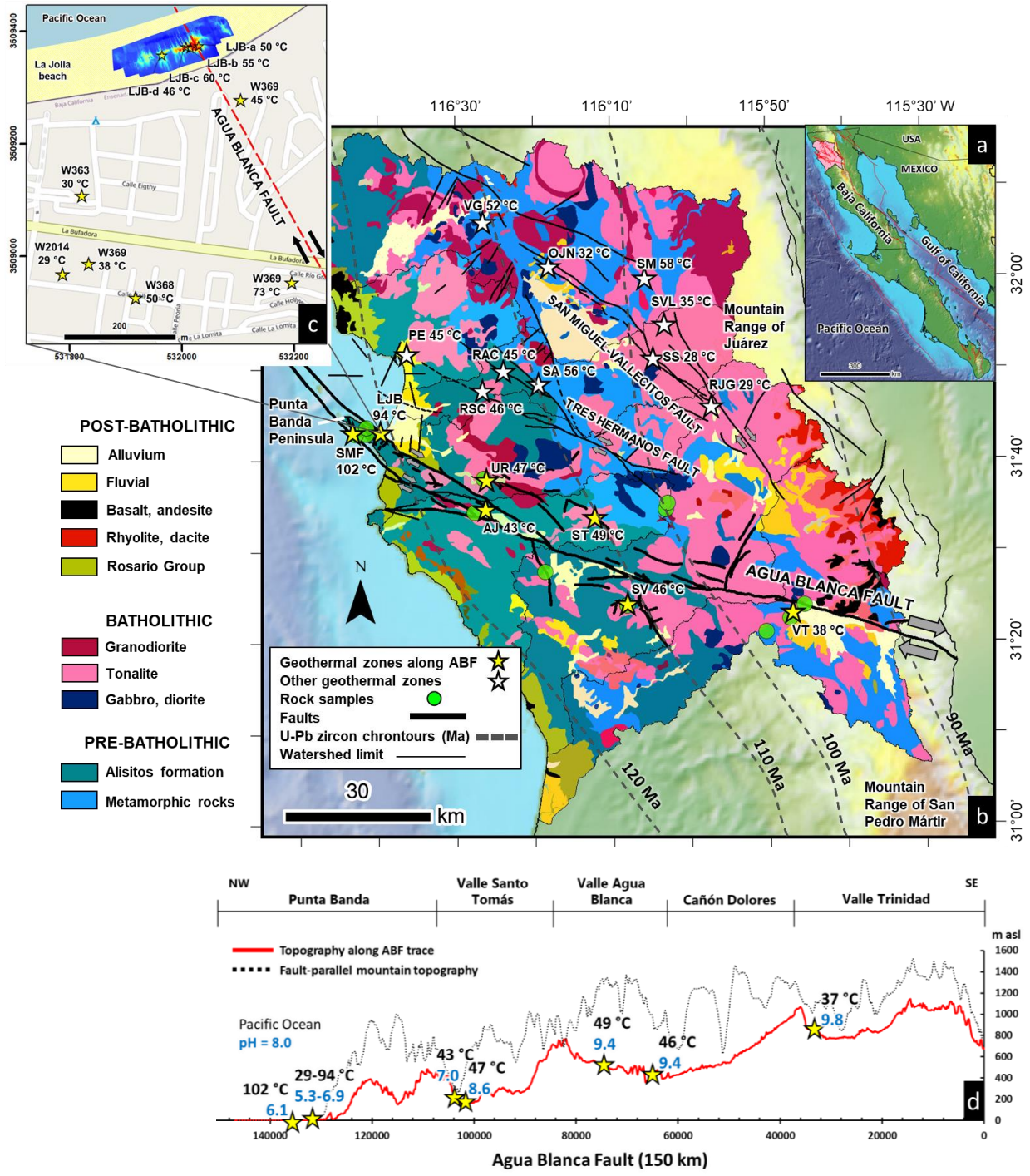

Figure 1. Locations of geological and geothermal features of the study area. a) Location of the study area (pink) in Ensenada, Baja California, Mexico. b) Geological map and location of seventeen orogenic amagmatic geothermal systems (stars) along fault traces (black lines). Map modified from Gastil et al. (1975). Yellow stars mark the thermal waters reported in this study.

Batholitic rocks are younger towards the east (dashed gray lines are U-Pb zircon chrontours from Ortega-Rivera, 2003). c) Detailed location of La Jolla beach thermal anomaly (Carbajal-Martínez et al., 2020) and surrounding domestic thermal wells. d) Amagmatic geothermal systems and topography along the main trace of the Agua Blanca Fault (ABF). Vertical scale is exaggerated for clarity. Dotted black line shows topography along a profile parallel to 3.5 km north of the Agua Blanca Fault.

153

154 ## 2 Materials and Methods

155 ### 2.1 Water sampling and analysis

156 Fourteen thermal waters (hot springs, domestic thermal wells, intertidal seeps) located
157 along the Agua Blanca Fault were sampled in 2018 and 2019. On-site measurements were made
158 for pH (to within ± 0.05 units with an OAKTON 150), temperature (to within ± 0.4 °C with a
159 HANNA HI 93503 thermocouple), and electrical conductivity (EC, to within ± 1% with a Thermo
160 Scientific Orion 105A conductivity meter). Samples were filtered through a 0.45 µm MILLIPORE
161 filter and collected in 50 mL High-Density Polyethylene (HDPE) bottles. Samples for cation
162 analysis were acidified using ultra-pure HNO_3. Alkalinity was determined on-site on filtered water
163 samples by titration with a 0.02 M H_2SO_4 solution using bromocresol green and phenolphthalein
164 as indicators.

165 Analyses were conducted at the geochemical laboratory of the Istituto Nazionale di
166 Geofisica e Vulcanologia–Palermo (INGV–PA), Italy. Anion concentrations were determined
167 using a Dionex ICS-1100 ion chromatograph and cations by Inductively Coupled Plasma Optical
168 Emission Spectroscopy (ICP-OES) with a Jobin Yvon Ultima 2 spectrometer. Analytical
169 uncertainty is ≤1% for concentrations above 1 meq L^{-1} and ≥5% for lower concentrations. Values
170 of $\delta^{18}O$ and $\delta^{2}H$ were determined by Continuous-Flow Isotope Ratio Mass Spectrometry (CF-
171 IRMS). For $\delta^{18}O$, a Thermo Delta V mass spectrometer was used, while $\delta^{2}H$ values were
172 determined using a Thermo Delta XP mass spectrometer. The isotopic ratios are expressed in δ-
173 notation (‰) relative to Standard Mean Ocean Water (SMOW). Uncertainties are less than ± 0.1‰
174 for $\delta^{18}O$ and ± 1‰ for $\delta^{2}H$.

175 ### 2.2 Gas sampling and analysis

176 Dissolved gases were sampled in 120 cm^3 glass flasks following the methodology of
177 Capasso & Inguaggiato (1998) and Inguaggiato & Rizzo (2004). The gas phase in equilibrium with

178 the water sample inside the glass flask was analyzed on an Agilent® 7890 gas chromatograph at
179 the INGV–PA to determine N_2, O_2, and CO_2 with an analytical uncertainty of ≤5%. The resulting
180 dissolved gas concentrations are reported in cm^3 STP g^{-1} H_2O (0 °C and 100 kPa) as calculated
181 using Bunsen coefficients (Table 2, Weiss, 1971; Capasso & Inguaggiato, 1998; Hamme &
182 Emerson, 2004).

183 Helium isotopes (^3He and ^4He), Ar, and ^{20}Ne dissolved in the water samples were analyzed.
184 The gas phase in equilibrium with the water sample inside the glass flask was analyzed with a
185 GVI-Helix® SFT mass spectrometer, yielding raw $^3He/^4He$ isotopic ratios, R_{raw}, to within >3%
186 analytical uncertainty. The R_{raw} ratios were normalized to the atmospheric ratio ($R_a = 1.40\times10^{-6}$;
187 Sano & Wakita, 1985) and reported as R_{raw}/R_a values (Table 2). Argon and Ne isotopes were
188 analyzed with Helix MC-GVI and Thermo Scientific Helix MC Plus mass spectrometers,
189 respectively, with analytical uncertainties <3%. The R_{raw}/R_a values were corrected for air
190 contamination (R/R_a) following Hilton (1996):
191

$$R/R_a = ((R_{raw} \times X) - 1) / (X - 1) \quad (1)$$

$$X = (^4He/^{20}Ne)/(^4He/^{20}Ne)_{air} \times (\beta_{Ne}/\beta_{He}) \quad (2)$$

192 where X is the air-normalized $^4He/^{20}Ne$ ratio of the dissolved gases, $(^4He/^{20}Ne)_{air} = 0.318$, β_{Ne} =
193 10.62, and β_{He} = 8.78 are Bunsen coefficients for solubility of Ne and He in pure water (Weiss,
194 1971) assuming that meteoric water recharge occurs at the average temperature of the study area
195 (17 °C).

196 **2.3 ^{4}He production rate and water residence times**

197 To estimate the average ^4He production rate in the study area, thirteen plutonic and volcanic
198 rocks representing the most abundant lithology and chemical composition of the entire study area
199 were sampled along the Agua Blanca Fault (Figure 1b). Rock samples were processed following
200 the Peters & Pettke (2017) methodology. This involved fine milling and pressing powder pills of
201 the samples before measuring the concentrations of major elements and the parent radionuclides
202 U and Th by Laser Ablation Inductively Coupled Plasma Mass Spectrometry (LA-ICP-MS) at the
203 University of Bern, Switzerland (Table S1, Electronic Appendix). A GeoLas-Pro 193 nm ArF
204 Excimer laser system (Lambda Physik, Göttingen, Germany) was used coupled with an ELAN
205 DRC-e quadrupole mass spectrometer (Perkin Elmer, Waltham, MA, USA). Data were reduced

using the SILLS software (Guillong et al., 2008). Average detection limits for SiO_2, Na_2O, K_2O, Th, and U are 0.0001 to 0.012 μg g^{-1}, and standard deviations of the concentrations are 0.034 to 0.536.

In crustal rocks, ^4He is produced from α-decay of ^{235}U, ^{238}U, and ^{232}Th, and it eventually dissolves into any groundwater present. Therefore, high ^4He concentrations typify groundwaters with long subsurface residence times (Andrews & Lee, 1979). In granitic rocks, the concentrations of U and Th are high, and dissolved ^4He concentrations may exceed the aqueous solubility of helium (Marine, 1979). Water residence times can be estimated from the ^4He production rate ($^4He_{pro}$) in the wall rocks along the groundwater flow path and the ^4He present in the thermal waters in excess of that due to equilibrium with the atmosphere upon recharge (Torgersen, 1980; Kulongoski et al., 2008). This excess ^4He, corrected for air contamination (cm^3 STP g^{-1} H_2O), is calculated as follows:

$$^4He_{ex} = {}^4He_s - {}^4He_{ASW} - ({}^{20}Ne_s - {}^{20}Ne_{ASW} \times (He/Ne)_{ASW}) \quad (3)$$

where ^4He_s and $^{20}Ne_s$ (cm^3 STP g^{-1} H_2O) are concentrations measured in the sample, $^4He_{ASW}$ and $^{20}Ne_{ASW}$ are the concentrations in pure air-saturated water at the mean annual recharge temperature of 17 °C (4.52×10^{-8} and 1.89×10^{-7} cm^3 g^{-1} H_2O, respectively), and $(He/Ne)_{ASW}$ is the He/Ne ratio in air-saturated water (0.2882, Weiss, 1971). When $^{20}Ne_s < {}^{20}Ne_{gASW}$, Eq. (3) reduces to

$$^4He_{ex} = {}^4He_s - {}^4He_{ASW} \times ({}^{20}Ne_{ASW}/{}^{20}Ne_s) \quad (4)$$

The He production rate ($^4He_{pro}$, cm^3 yr^{-1} g^{-1} H_2O) is defined as

$$^4He_{pro} = \rho_r \Lambda \times (1.19 \times 10^{-13} \times U + 2.88 \times 10^{-14} \times Th) \times (1 - \phi)/(\phi) \quad (5)$$

where ρ_r is the bulk density of the wall rock (g cm^{-3}), ϕ is the fracture porosity through which advective water flow occurs, Λ is the fraction of He produced in the rock that is subsequently released into the groundwater (here Λ is assumed to be equal to 1), and U and Th are the uranium and thorium concentrations in the rock (μg g^{-1}), with decay rates of 1.19 x 10^{-13} and 2.88×10^{-14} cm^3 STP ^4He yr^{-1} μg^{-1}, respectively (Kulongoski et al., 2008). To solve Eq. (5), we used the average

concentrations of 1.2 μg g^{-1} U and 4.9 μg g^{-1} Th in the rocks along the ABF (Table S1, Electronic Appendix). Ignoring any deep crustal flow entering the system, the water residence time is given by the ratio $^4He_{ex}/^4He_{pro}$ (Eqs. 3–5).

2.4 Seismic hypocenters and rheological models

We interpreted earthquake data using standard rheological models to estimate the depth to the brittle–ductile transition zone (BDTZ) and the regional geothermal gradients along the ABF. Hypocenters of 116 seismic events on the ABF with magnitudes of 1–3.3 and hypocentral uncertainties <60% were selected from RESNOM (2017), and 74 events with magnitudes of 1.5–2.1 and hypocentral uncertainties <1 km were taken from Frez et al. (2004). Seismic epicenters along the ABF are shown in Figure S1 in the Electronic Appendix.

Brittle behavior was modeled by Byerlee's law and ductile behavior by Power Law Creep (Eqs. 6 and 7, respectively) for crustal rocks (Byerlee, 1978; Brodi & Iizuka, 1993; Van der Pluijm & Marshak, 2004):

$$\tau = 0.68\sigma_n \quad (6)$$

where τ is the shear stress, σ_n is the normal stress (MPa), 0.68 is the coefficient of friction at the center of the Byerlee range (Byerlee, 1978), and

$$\sigma_d = [\dot{\varepsilon}/A_1]^{1/n} \exp[E^*/nRT] \quad (7)$$

where σ_d is the differential stress (MPa), $\dot{\varepsilon}$ is the strain rate (s^{-1}), A_1 is a material constant (MPa^{-n} s^{-1}), E^* is the activation energy (kJ mol^{-1}), n is the stress exponent (dimensionless), R is the gas constant (8.31 J mol^{-1} K^{-1}), and T is the temperature (°C).

Deformation becomes ductile at depths greater than the BDTZ (corresponding to pressure >200 MPa and temperature = 300–450 °C). Since earthquakes represent brittle responses to stresses in the crust, the BDTZ can be located from the depth at which seismic events become infrequent (Brodi & Iizuka, 1993; Dragoni, 1993; Stober et al., 2016). Therefore, we assumed that the BDTZ lies at the minimum depth encompassing 95% of post-2001 seismic events.

To solve Eq. 7 for the ABF we used the experimental values of wet granite: n = 1.9, E^* = 137 kJ mol^{-1}, $A_1 = 2.0 \times 10^{-4}$ MPa^{-n} s^{-1} (Twiss & Moores, 1992). Further, we used a strain rate of 1.01×10^{-12} s^{-1}, consistent with the observed shear strain rate of the ABF of 3.2 mm yr^{-1} (Wetmore et al., 2018), and we assumed a deformation zone width of 0.1 km (this width is 0.07% of the

length of the ABF). Finally, to derive geothermal gradients, we varied the temperature until Eq. 7 intersected Eq. 6 at the deduced depth of the BDTZ.

3 Results

3.1 Water chemistry

Amagmatic orogenic geothermal systems along the ABF host three to six hot springs. Table 1 lists the physicochemical parameters of the sampled thermal waters. Towards the west along the fault, discharge temperatures increase from 37 to 102 °C, while pH decreases from 9.8 to 5.3 (Figure 1d). The total concentrations of dissolved solids (TDS) show a remarkably wide variation, which divides the samples into two geographic groups: inland versus coastal–submarine (Table 1). The inland samples are located far from the ocean (>30 km, Figure 1d) and have low TDS of 0.3–0.9 g L^{-1}, whereas the coastal–submarine samples are more saline with TDS of 8–19 g L^{-1}. The coastal–submarine group includes waters from six shallow domestic thermal wells, the coastal thermal anomaly at La Jolla beach (Figure 1c), and the fumarolic submarine field. Sodium and Cl dominate the solutes in all thermal waters, but compared to seawater, the coastal–submarine samples are enriched in Ca, Li, B (Figure 2a), and SiO_2. All thermal water samples show a strong linear correlation between Na and Cl concentrations (R^2 = 0.99; Figure 2b), reflecting binary mixing with seawater. In contrast, Mg concentrations are depleted in the coastal–submarine samples compared to the binary seawater mixing line (Figure 2c), demonstrating that Mg does not behave conservatively.

3.2 Stable O–H isotopes of thermal waters

Values of $\delta^{18}O$ and $\delta^{2}H$ in the thermal waters range from -3.5 to -8.5‰ and -25.4 to -61‰, respectively (Table 1). Inland samples fall in the range of $\delta^{18}O$ and $\delta^{2}H$ values in modern rainfall in southern California and Baja California (Kretzschmar & Frommen, 2013; Williams & Rodoni, 1997) and have delta values lower than coastal–submarine samples and local seawater (in which $\delta^{18}O$ is -0.6 and $\delta^{2}H$ is -3.5‰; Figure 2d). Most thermal water samples plot close to the Global Meteoric Water Line (GMWL, Craig, 1961), demonstrating their meteoric origin. The deviation from the GMWL observed for the coastal–submarine waters is consistent with the admixture of seawater, in accord with the correlations between Na and Cl concentrations (Figure 2b) and between $\delta^{2}H$ and Cl values (Figure 2e).

To estimate the fraction of admixed seawater (F_{sw}) in the coastal–submarine samples, we assume a binary mixing model:

$$F_{sw} = (Cl_{tw} - Cl_{mw}) / (Cl_{sw} - Cl_{mw}) \quad (8)$$

where Cl_{tw} is the Cl concentration measured in the thermal water sample, and Cl_{mw} and Cl_{sw} are the concentrations of Cl in meteoric water and seawater, respectively. Given the low Cl concentrations in the inland waters, we assume that the meteoric water is Cl-free for this calculation, and we use our measured Cl concentration in local seawater (18,967 mg L^{-1}, Table 1) as a seawater endmember. This mass balance reveals that the coastal–submarine samples contain between 25 and 57 mass% seawater (Table S2, Electronic Appendix). These fractions allow reconstruction of the initial isotopic signatures of the coastal–submarine samples before their mixing with seawater ($\delta^{18}O_i$ and $\delta^{2}H_i$), e.g., for oxygen:

$$\delta^{18}O_i = (\delta^{18}O_{tw} - F_{sw} \times \delta^{18}O_{sw}) / (1 - F_{sw}) \quad (9)$$

Figure 2f shows the initial $\delta^{18}O_i$ and $\delta^{2}H_i$ values for the coastal–submarine samples (Table S2, Electronic Appendix), which are close to the inland thermal waters and the GMWL. The same binary mixing model was used to calculate the theoretical discharge temperature of the thermal springs to correct for cooling caused by the admixture of seawater. This resulted in unmixed discharge temperatures between 33 and 212 °C for the coastal–submarine samples (Table S2, Electronic Appendix).

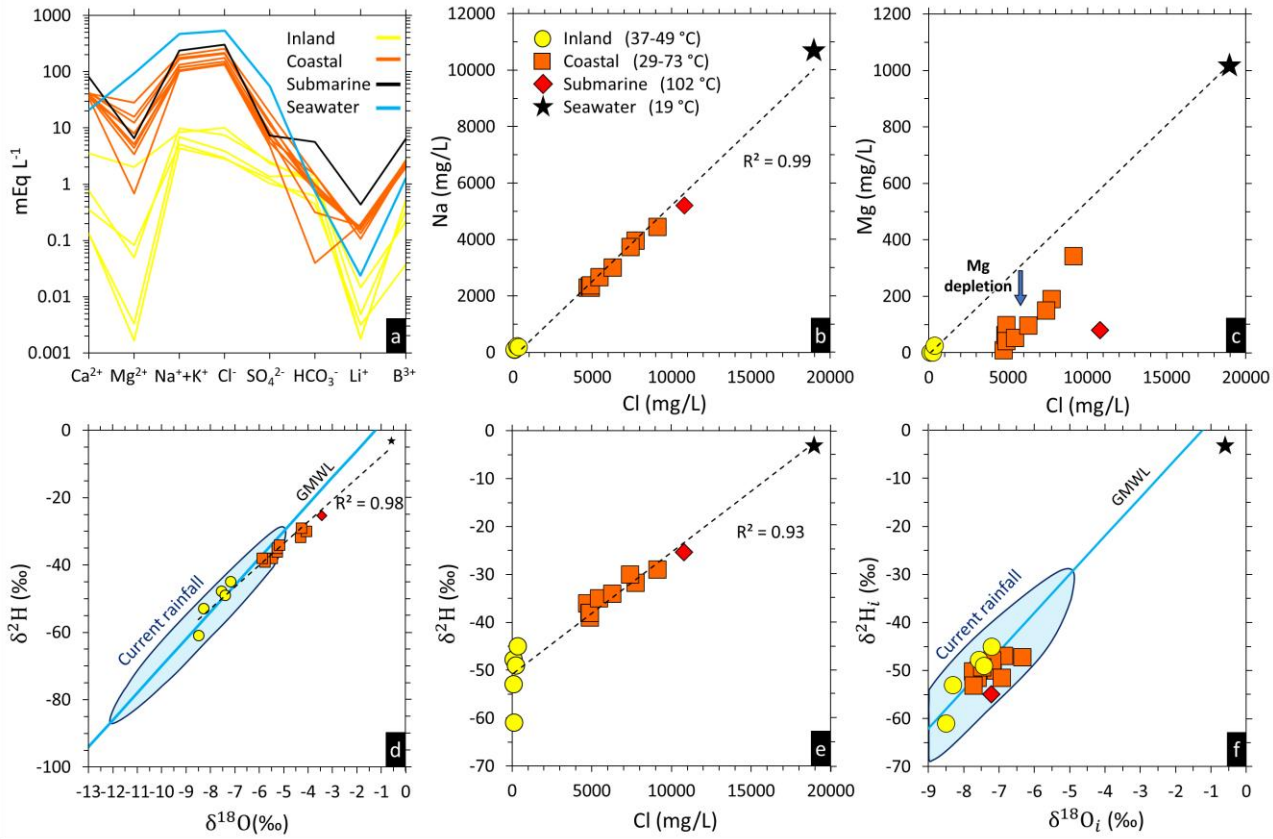

Figure 2. Element and stable O–H isotope correlations in thermal water samples. a) Schoeller diagram of thermal waters sampled along the Agua Blanca Fault. b) Sodium vs. chlorine concentrations indicating binary mixing between seawater and thermal waters. All the thermal water samples were considered to estimate the R^2 = 0.99. c) Magnesium vs. chlorine concentrations illustrating the Mg depletion of coastal–submarine samples compared to the conservative mixing trend with seawater. d) Plot of $\delta^{18}O$ vs. $\delta^{2}H$ indicating that the thermal waters are of meteoric origin. Current rainfall is from southern California, and Baja California is represented by a blue oval (Williams & Rodoni, 1997; Kretzschmar & Frommen, 2013). e) Plot of $\delta^{2}H$ vs. Cl showing that the coastal–submarine waters contain admixed seawater. f) Initial values of O–H isotopes ($\delta^{18}O_i$ and $\delta^{2}H_i$), with coastal–submarine waters corrected for the admixture of seawater (see text; exact values provided in Table S2, Electronic Appendix). GMWL: global meteoric water line (Craig, 1961).

313

Table 1

Chemical and isotopic compositions of thermal waters collected along the Agua Blanca Fault, Ensenada, Baja California, Mexico. Concentrations are given in mg L^{-1}. Total Dissolved Solid concentration (TDS) is given in g L^{-1}. Stable isotope ratios are expressed as δ values (‰) relative to SMOW.

Class	Type	Sample	T (°C)	pH	TDS	Na^+	K^+	Mg^{2+}	Ca^{2+}	Li^+	Cl^-	SO_4^{2-}	Br^-	HCO_3^-	F^-	SiO_2	$\delta^{18}O$	δ^2H
Inland	Spring	VT	37	9.8	0.51	156	1.9	0.04	2.65	33	137	66	bdl	90	2.1	53.5	–8.5	–61.0
		SV	46	9.4	0.34	100	1.1	0.02	2.7	22	100	59	bdl	27	3.3	45.9	–7.6	–47.8
		ST [b]	49	9.4	0.37	118	1.5	1.0	7.1	NM	105	49	bdl	38	11.6	41.4	–8.3	–53.0
		UR	47	8.6	0.75	225	3.1	0.6	15.2	100	266	121	0.8	61	4.5	52.7	–7.4	–49.0
	Well	AJ	43	7.0	0.88	192	3.2	24.6	70.7	12	357	113	1.1	72	1.8	43.3	–7.2	–45.0
Coastal	Wells at La Jolla	W368	50	6.9	8.60	2341	93.6	61.8	766.3	1126	4849	386	15.5	56		48.0	–5.5	–38.0
		W369	73	5.3	8.11	2289	112.0	8.2	685.1	1355	4714	231	17.3	2.4		68.8	–5.3	–36.0
		W363	30	6.5	8.63	2208	93.6	61.8	766.3	1149	4849	386	bdl	56		74.9	–5.8	–38.0
		W2014	29	6.2	8.53	2294	82.2	97.8	700.4	924	4894	312	bdl	90		63.0	–5.8	–39.0
		W367	38	6.5	8.52	2370	100.5	41.6	729.6	1171	4888	264	bdl	49	bdl	75.5	–5.9	–38.0
		WAGC	45	6.4	9.50	2659	108.7	53.1	802.1	1255	5442	332	bdl	20		85.8	–5.3	–35.0
	Thermal anomaly La Jolla beach	LJB-a	50	6.8	13.63	3961	145.6	190.0	832.9	1089	7738	614	23.7	46		82.8	–4.3	–31.7
		LJB-b	55	6.7	12.99	3733	140.5	150.2	846.9	1120	7396	557	21.7	61		87.3	–4.1	–30.0
		LJB-c	60	6.4	10.86	3002	122.1	95.8	786.2	1183	6279	420	21.3	46		87.2	–5.2	–34.0
		LJB-d	46	6.9	15.96	4440	161.4	342.6	819.7	743	9120	904	33.4	90		53.1	–4.3	–29.0
Submarine	Vent	SMF [b]	102	6.1	18.95	5200	410.0	80.0	1600.0	3000	10800	351	NM	347	1.8	156	–3.5	–25.4
Seawater	Seawater	SW	19	8.1	34.20	10729	329.9	1021.3	413.0	165	18967	2610.2	67.4	45	bdl	2.3	–0.6	–3.0

bdl: Data below detection limit;
NM: not measured;
[b] Data from Vidal et al. (1981) and Zúñiga (2010).

3.4 Gas chemistry of thermal waters

Nitrogen is the dominant gas dissolved in the thermal waters, with concentrations (1.0–2.3 × 10^{-2} cm^3 STP g^{-1} H_2O, Table 2) mostly higher than that in air-saturated water ASW (1.2 × 10^{-2} cm^3 STP g^{-1} H_2O, Table 2). The volume ratios of N_2/Ar in inland and coastal thermal waters (10–38) approach that in ASW (38.6). In contrast, the submarine sample SMF has an N_2/Ar ratio of 160. According to Vidal et al. (1982), such a value may originate from the decomposition of nitrogenous compounds in sediments. The second most abundant gas is O_2, which has a lower concentration (1.4–25 × 10^{-4} cm^3 STP g^{-1} H_2O) than ASW (66 × 10^{-4} cm^3 STP g^{-1} H_2O). Depletion in O_2 is likely due to its reduction by reaction with wall rocks during deep fluid circulation. Most of the thermal waters have lower CO_2 concentrations (0.1–0.3 × 10^{-3} cm^3 STP g^{-1} H_2O) than ASW (0.3 × 10^{-3} cm^3 STP g^{-1} H_2O). The exceptions are three samples from shallow wells W368, W369, and AJ, which have higher values (4–17 × 10^{-3} cm^3 CO_2 STP g^{-1} H_2O), presumably due to microbial activity in the wells.

Concentrations of ^{4}He range from 0.6–6.2 × 10^{-6} cm^3 STP g^{-1} H_2O (Table 2) and are up to 13–136 times higher than ASW (4.55 × 10^{-8} cm^3 STP g^{-1} H_2O). The volume ratios of ^{4}He/^{20}Ne are 7–92 times higher than those measured in ASW (0.28). The concentrations of ^{4}He and ^{20}Ne in coastal samples were recalculated (Table 2) assuming binary mixing with air-saturated seawater (ASSW), using the He and Ne concentrations in ASSW at 17 °C (3.83 × 10^{-8} and 1.60 × 10^{-7} cm^3 g^{-1} H_2O; Sano & Takahata, 2005) and the estimated seawater fractions (Table S2, Electronic Appendix).

The ^{3}He/^{4}He ratios were corrected for air contamination and seawater mixing (R) and normalized to the value of air (denoted R/R_a), ranging from 0.06 to 0.94. The coastal samples contain the lowest ^{4}He concentrations (0.6–1.7 × 10^{-6} cm^3 STP g^{-1} H_2O), ^{4}He/^{20}Ne ratios (2–5), and R/R_a ratios (0.06–0.26). As helium shows negligible isotopic fractionation during water–gas interaction, the R/R_a value can be used to track the origin of the gas in terms of the air, mantle, and crust endmembers. Figure 3 shows R/R_a versus ^{4}He/^{20}Ne ratios for ASW (R/R_a = 1), radiogenic crust ($R_r = (R/R_a)_{radiogenic}$ = 0.015, Sano & Wakita, 1985), and the mantle as represented by MORB (Mid-Ocean Ridge Basalt). For the MORB endmember, we used the highest R/R_a value measured in the Alarcón basin in the nearby Gulf of California ($R_m = (R/R_a)_{MORB}$ = 8.38; Castillo et al., 2002). Figure 3 indicates that He dissolved in the thermal waters derives mainly from radiogenic decay.

348 The fractions of mantle helium (F_m) in the waters are calculated from the R values in Table
349 2 with the following equation (modified from Sano & Wakita, 1985):
350

$$F_m = (R - R_r) / (R_r + R_m) \quad (10)$$

351
352 with the remainder ($1 - F_m$) being equal to the fraction of radiogenic helium (F_r). This shows that
353 mantle He makes up less than 11% of the total He in the samples (Figure 3). Notably, the lowest
354 mantle contributions (0.6–2.9%) are found in the coastal samples (Table 2). Owing to the lack of
355 ^{20}Ne analyses of the submarine sample SMF (Vidal et al., 1982) and ^{3}He/^{4}He analysis of the
356 subaerial sample ST (Zúñiga, 2010), their mantle and radiogenic He contributions cannot be
357 estimated.

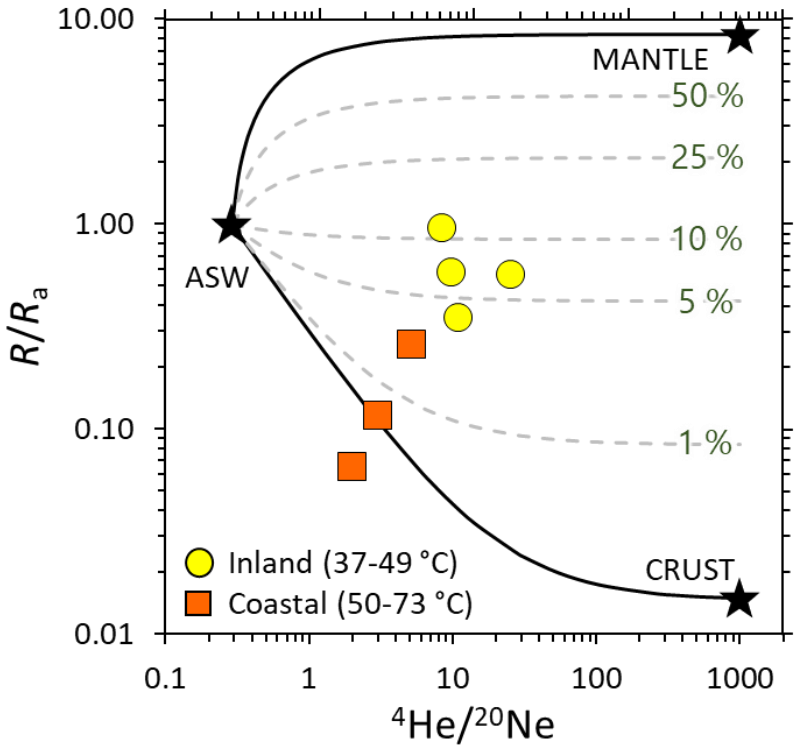

Figure 3. Helium–neon isotopic composition (R/R_a vs. ^{4}He/^{20}Ne) of inland and coastal thermal waters along the Agua Blanca Fault. Compositions of mantle, crust and air are plotted as endmembers (logarithmic axes). Dashed lines are the mantle contributions in the samples.

358

3.5 Water residence times

To estimate the residence times of the thermal waters in the ABF from Eq. 5, we assumed a somewhat arbitrary fracture porosity of 1%. This falls within the 0.1–2% range found in deep borehole hydraulic tests in the granite–gneiss basement of southern Germany (Stober & Bucher, 2007). The resulting calculated residence times for the ABF samples span 5–83 kyr (Table 2). Within this span, the coastal samples have significantly shorter residence times (5–15 kyr) than the inland samples (28–83 kyr). As there are no hydraulic measurements in the study area, these times are subject to unknown and possibly large errors (e.g., 100% or more). However, the relative age difference between coastal and inland waters is likely to be robust.

Table 2

Chemical and isotopic compositions of gases dissolved in thermal waters (DG, expressed in cm^3 STP g^{-1} H_2O) and bubbling gases (BG expressed in volume %) along the Agua Blanca Fault.

Sample	Type	N_2 ($\times10^{-2}$)	O_2 ($\times10^{-4}$)	CO_2 ($\times10^{-3}$)	^4He ($\times10^{-6}$)	^{20}Ne ($\times10^{-7}$)	$^4He_{ex}$ ($\times10^{-6}$)	N_2/Ar	$^4He/^{20}Ne$	R_{raw}/R_a [a]	$\pm R/R_a$ [b] ($\times10^{-3}$)	R/R_a [c]	F_m [d] (%)	F_r [e] (%)	Age [f] (kyr)
VT [g]	DG	1.50	1.37	0.33	4.35	1.68	4.85	28.4	25.9	0.57	6.1	0.56	6.6	93.4	66
SV [g]	DG	2.30	6.39	0.10	4.88	5.75	4.72	13.9	8.5	0.95	9.6	0.94	11.1	88.9	65
UR [g]	DG	1.79	6.61	0.27	6.23	6.34	6.06	9.8	9.8	0.59	8.4	0.58	6.7	93.3	83
AJ [g]	DG	1.65	1.66	17.0	2.10	1.88	2.07	37.8	11.2	0.36	6.6	0.35	4.0	96.0	28
W369	DG	1.00	25.3	4.37	0.81 [h]	2.67 [h]	0.56	32.1	3.0	0.19	7.1	0.12 [h]	1.2	98.8	8
W368	DG	1.30	6.20	13.8	0.56 [h]	2.76 [h]	0.36	33.8	2.0	0.19	9.1	0.06 [h]	0.6	99.4	5
LJB-c	DG	NM	NM	NM	1.70 [h]	3.22 [h]	1.07		5.2	0.29	4.6	0.26[h]	2.9	97.1	15
SMF [i]	BG	56.1	0.29	1.8	0.08	NM		160		0.54					
ASW [i]		1.23	66.0	0.31	0.045	1.63		38.6	0.28						

[a] Raw measured $^3He/^4He$ ratio (R_{raw}) normalized to the $^3He/^4He$ ratio of air (R_a);
[b] Uncertainty in R_{raw}/R_a;
[c] $^3He/^4He$ ratio (R) corrected for air contamination and normalized to the $^3He/^4He$ ratio of air (R_a);
[d] Fraction of mantle He (see text);
[e] Fraction of radiogenic He (see text);
[f] Water residence times derived from Eqs. (3–5);
[g] Inland samples. Other samples are coastal (W369, W368, LJB-c) or submarine (SMF).
[h] Concentrations and isotopic values corrected for admixed seawater based on fractions in Table S2 (Electronic Appendix) and air-saturated seawater values (see text);
[i] Values of SMF from Vidal et al. (1981) and air-saturated water values from Capasso & Inguaggiato (1998);
NM: not measured.

3.6 Brittle–ductile transition zone and geothermal gradient

Based on the rheological and hypocenter analysis in Section 3.4, Figure 4 shows the calculated depths to the brittle–ductile transition zone (BDTZ) and the geothermal gradients for three geographic segments of the ABF. Thus, from NW to SE towards the mountainous zones, the BDTZ lies at progressively greater depths (from 12 through 15 to 18 km), and the geothermal gradient becomes progressively lower (from 24 through 18.7 to 15.2 °C km^{-1}). The low geothermal

gradient in the mountainous area (15.2 °C km^{-1}) is consistent with that measured in a well 40 km southeast of the ABF in the San Pedro Mártir range (14.9 °C km^{-1}; Smith et al., 1979). The estimated geothermal gradients are typical of average crust in amagmatic regions elsewhere, as expected from the absence of volcanism since the Miocene and the >90 Ma age of the local intrusive rocks (Storey et al., 1989; Ortega-Rivera, 2003). This is confirmed by the low heat flow values reported for Southern California (< 60 mW m^{-2}, Erkan & Blackwell, 2009), consistent with the subduction of the Farallon plate having ceased more than 30 Ma ago (Atwater, 1970).

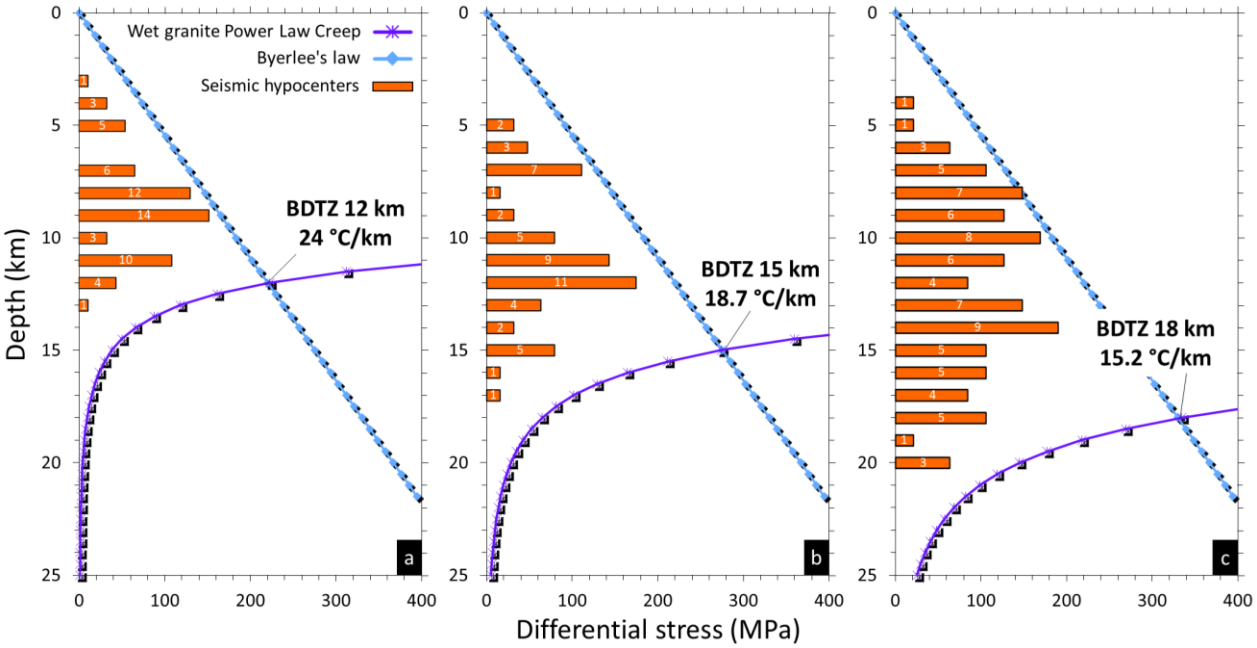

Figure 4. Rheological models and histograms of seismic hypocenters versus depth along three geographic segments of the Agua Blanca Fault (ABF). The brittle–ductile transition zone (BDTZ) is placed at the minimum depth that encompasses 95% of the plotted post-2001 seismic events (Frez et al., 2004; RESNOM, 2017). The indicated geothermal gradients were obtained by fitting the intersection of Byerlee's Law and Power-Law Creep for wet granite (blue vs. purple lines, respectively) to the BDTZ (see text). (a) NW segment of the ABF: Punta Banda to part of the Santo Tomás Valley. (b) Central segment of the ABF: Valle Santo Tomás – Valle Agua Blanca – Cañon Dolores – NW part of Valle Trinidad. (c) SE segment of the ABF: SE part of Valle Trinidad to between the San Pedro Mártir and Sierra Juárez mountain ranges. Locations of the three segments in subfigures (a–c) are shown in Figure 1d.

3.7 Minimum temperature and depth of water–rock equilibration

The Peninsular Ranges Batholith of Baja California is dominantly tonalite and granodiorite, hence it contains abundant feldspar and quartz. This permits the assumption that the aqueous concentrations of Na, K, and SiO_2 are buffered by reactions with these minerals at high temperatures along the deep water flow paths. Thus, classical solute geothermometers can provide constraints on the temperatures attained by the thermal waters during their circulation within the Agua Blanca Fault system. For the equilibrium

$$\text{Albite} + K^+ \rightleftharpoons \text{K-feldspar} + Na^+ \quad (11)$$

the temperature dependency of the molar Na/K concentration ratio is taken from Giggenbach (1988):

$$T_{Na/K}\ (°C) = (1390 / \log (Na/K + 1.75)) - 273.15 \quad (12)$$

Similarly, for the quartz equilibrium

$$\text{Quartz} \rightleftharpoons SiO_{2(aq)} \quad (13)$$

Fournier & Potter (1982) determined the temperature dependency at low to moderate pH values as follows:

$$T_{quartz}\ (°C) = -42.198 + 0.28831[SiO_2] - 3.36686 \times 10^{-4}\,[SiO_2]^2 + 3.1665 \times 10^{-7}\,[SiO_2]^3 + 77.034 \times \log [SiO_2] \quad (14)$$

In equation (14), $[SiO_2]$ refers to the silica concentration in mg L^{-1}.

Fournier (1977) determined that at lower temperatures (<110 °C), other silica phases, such as chalcedony, may control the dissolved silica concentration:

$$T_{chalcedony}\ (°C) = 1032 / 4.69 - \log [SiO_2] \quad (15)$$

In equation (15) $[SiO_2]$ refers to the silica concentration in mg L^{-1}.

Water–mineral reactions typically slow down during the ascent and cooling of thermal water, causing it to deviate from the equilibrium state. This implies that the metastable solute concentrations measured in surface springs (Table 1) represent their values when the water was last in equilibrium with the buffering minerals (Fournier et al., 1973). Given that reaction kinetics change only gradually and that rock temperatures become progressively higher with depth, the reconstructed equilibration temperatures are considered minimum estimates.

The minimum equilibration temperatures obtained from the Na/K, quartz, and chalcedony geothermometers are shown in Figure 5. The quartz and chalcedony geothermometers should not be applied to the inland samples (dashed red and green lines in Figure 5) because their pH is up to 9.8, causing an increase in silica solubility that is not captured by the geothermometer calibration in Eq. 14 and 15. On the other hand, in the coastal–submarine thermal waters, the molar Na/K ratios of 13–28 dominantly reflect admixture of seawater (molar $Na/K_{seawater}$ = 33) rather than buffering by albite and K-feldspar, thereby precluding the application of the Na/K geothermometer (dashed black in Figure 5). To solve the latter issue, we used the quartz and chalcedony geothermometers (Eq. 14, 15) to estimate the equilibration temperature of the coastal–submarine thermal waters. To account for mixing with seawater, we used a binary mixing model with the derived seawater fractions and the seawater SiO_2 concentration of 2.3 mg L^{-1} to estimate the SiO_2 concentration in the thermal endmember water via Eqs. 14 and 15 (Table S2, Electronic Appendix).

The minimum equilibrium temperatures for inland geothermal systems are between 103 and 121 °C (Na/K geothermometer), increasing from southeast to northwest along the ABF (Figure 5). In contrast, the minimum equilibrium temperatures for the coastal–submarine systems are 84 to 209 °C (chalcedony geothermometer). The hottest values are in the coastal geothermal anomaly at La Jolla beach and the fumarolic submarine field (133 and 209 °C, respectively, chalcedony geothermometer).

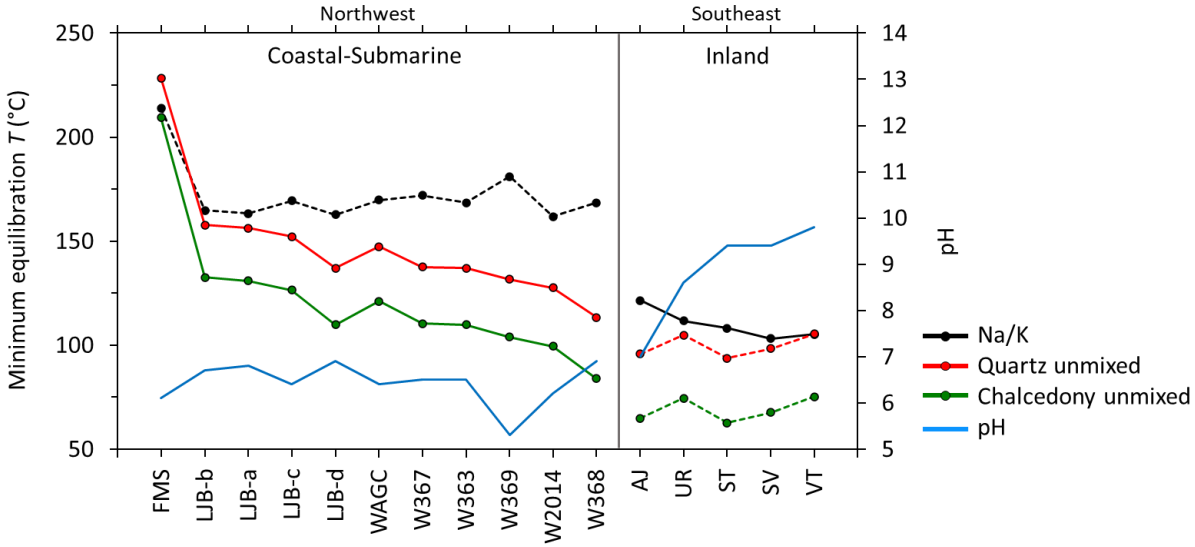

Figure 5. Minimum temperatures of the thermal waters at depth along the Agua Blanca Fault from NW to SE, based on Na/K and $SiO_{2(aq)}$ geothermometry (see text for interpretation). Also shown are pH values measured at the temperature of discharge (right-hand *y* axis).

To estimate the minimum depth at which the thermal waters equilibrated with their wall rocks ($z_{eq,min}$), we used the Na/K temperature for the inland samples and the unmixed quartz temperatures for the coastal-submarine samples (T_{Geot}, Table S3, Electronic Appendix) in combination with Eq. (16):

$$z_{eq,min} = (T_{geot} - T_{amb}) / (\Delta T/\Delta z) \quad (16)$$

where T_{amb} refers to the average ambient temperature of 17 °C, and $\Delta T/\Delta z$ is the geothermal gradient in the relevant segment of the ABF as derived from the rheological models (Figure 4). The resulting equilibration depths are 4.6–8.8 km (Table S3, Electronic Appendix). Figure 6 demonstrates that the coastal–submarine samples in the west (with discharge temperatures > 60 °C) have the highest minimum equilibration depths (5.9–8.8 km), whereas the cooler inland samples in the east (with discharge temperatures < 50 °C) have the lowest minimum equilibration depths (4.6–5.6 km).

It should be noted that choosing the quartz temperature to estimate the equilibration depth of the coastal–submarine samples is arbitrary. From scaling in geothermal wells it has been shown that owing to kinetic limitations, quartz only forms at temperatures >180 °C while chalcedony may form down to a temperature of about 110 °C (Arnorsson, 1975). However, when the water upflow rate and the reactive fracture surface area are low, such as in long-lived active geothermal systems, quartz can also form at <100 °C (White et al., 1956; Rimstidt & Barnes, 1980). Due to the lack of deep samples, we do not know which silica phase controls the SiO_2 concentrations measured in the sampled thermal waters. Consequently, the equilibration depth listed for the coastal-submarine samples (Table S3, Electronic Appendix) could be up to 1 km less (the equilibration temperature of chalcedony is about 25 °C less for the same SiO_2 concentration).

4 Discussion

A conceptual model of the amagmatic orogenic geothermal systems along the ABF, consistent with all geological, geochemical, and geophysical data presented above, is illustrated in Figure 6. Topographic potential drives the infiltration of meteoric water from high altitudes deep into the basement but not beyond the brittle–ductile transition zone. Variations in permeability and hydraulic head gradients lead to variable water penetration depths, water equilibration temperatures, and water upflow velocities. Consequently, there is a large range in temperatures (37–102 °C) of discharges in topographic lows where the local hydraulic head gradients are highest. Additionally, the chemical composition of meteoric water changes along its flow path due to long water residence times and mixing processes with ancient seawater-like porewater as well as mineral precipitation and dissolution. In the coastal systems, mixing with fresh seawater also occurs. All these processes are discussed in detail in the following sections.

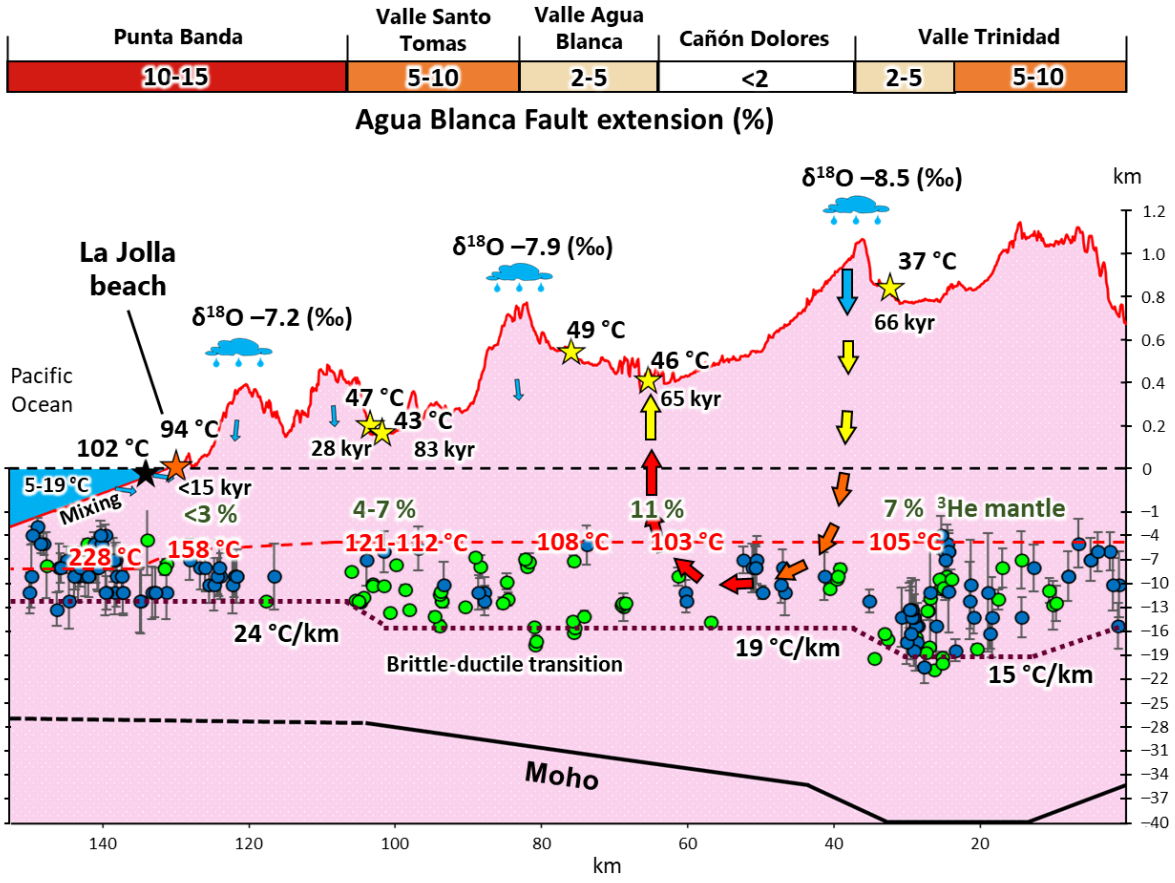

Figure 6. Conceptual model of amagmatic geothermal systems hosted by the Agua Blanca Fault (stars), projected into a long section along the trace of the fault (red line). Note the differences

between the horizontal scale and the two-part vertical scale. Colored bands at the top show extension as a fraction of total displacement (%) along five geographic segments of the fault (Wetmore et al., 2019). At higher altitudes, rainwater precipitation is higher, colder, and has lighter $\delta^{18}O$. Surface topography drives the penetration of meteoric water possibly as deep as the brittle–ductile transition zone, during which it heats up along the local geothermal gradient (15–24 ºC/km). Subsequent ascent of the heated water leads to discharge at low points in the topography, corresponding to the highest local hydraulic head gradients. Discharge temperatures (black numbers in °C), residence times (black numbers in kyr), and percentages of $^{3}He/He_{total}$ (grey numbers) depend on the permeability (fault extension) of the upflow zone below the discharge locations (see text) and the hydraulic head gradient. Salinity of the infiltrated meteoric water increases along the flow path as seawater-like porewater is released from the rock matrix into the hydraulically active fracture network. In coastal areas, admixture of modern seawater also increases the salinity of the ascending thermal waters. Seismic events are represented by green (Frez et al., 2004) and blue circles (RESNOM, 2017) with vertical error bars. Red dotted line: depth and temperature at which ascending water departs from chemical equilibrium with its wall rocks. Purple dashed line: depth of brittle–ductile transition zone and its local geothermal gradients (black numbers in °C/km), which are deeper and colder, respectively, depending on Moho depth (black line; Reyes et al., 2001).

4.1 Evolution of chemical composition along the meteoric water flow path

The chlorine concentration in the infiltrated meteoric water along the ABF has increased from its typical original value of <2 mg L^{-1} (Junge & Werby, 1958) to 100–360 mg L^{-1} in the inland thermal springs and 4700–11000 mg L^{-1} in the coastal–submarine springs. Water–rock interaction along flow paths is known to increase the concentrations of solutes in infiltrating meteoric water (López & Smith, 1995). Additionally, sea spray may elevate chloride concentrations in meteoric water in the coastal zone and up to 20 km inland (Tsunogai, 1975).

Possible sources of Cl can be constrained by examining the Cl/Br concentration ratios in the spring waters. Along the ABF the Cl/Br mass ratios are 273–338, close to that of seawater in the study area (280). The inland recharge areas are too far from the coast to be affected by sea spray, but pore spaces in the deep host rocks of the ABF likely contain fossil seawater. Thus, during the migration of meteoric water along fracture networks in the fault system, Cl and Br, and

likely also some Na, Mg, SO_4, and Li, are assumed to have been acquired by diffusive or advective mixing with seawater-like porewater (e.g., Waber & Smellie, 2008; Waber et al., 2017). Hence, the Cl concentration in the thermal waters depends on their effective cumulative water/rock ratios, which in turn are a function of residence time, path length, porewater chlorinity, volume of accessible pore spaces, and surface area of fractures that allow exchange between the circulating meteoric water and the rock matrix. During upflow of the thermal meteoric water in the coastal area, shallow mixing with modern seawater occurs. Assuming that the chlorinity of the deep waters in the coastal zone was originally similar to that of the inland thermal waters (~300 mg L^{-1}, Table 1), binary mixing calculations yield approximately 25–57% modern seawater in the coastal springs.

Other chemical processes that increase the concentration of solutes are mineral dissolution and precipitation reactions along the water flow path, which increase the concentrations of SiO_2, B, F, and Ca. For example, the SiO_2 concentration is typically controlled by the solubility of either quartz or chalcedony (Fournier & Potter, 1982; Olguín-Martínez et al., 2022). On the other hand, B and F enrichments are caused by the dissolution of silicate minerals such as biotite, muscovite, and tourmaline (Seelig & Bucher, 2010), and Ca concentrations are controlled by plagioclase weathering and dissolution or precipitation of secondary calcite (Seyfried & Bischoff, 1979). Finally, the admixture of Mg by seawater in the coastal–submarine thermal waters leads to the precipitation of Mg-bearing sheet silicates (Stober & Bucher, 1999), causing the observed depletion of Mg in the fluid (Figure 2c).

4.2 Infiltration of meteoric water and hydraulic head gradients

Stable isotopes of water are fractionated during condensation from cloud vapor. As a result, $\delta^{18}O$ and $\delta^{2}H$ values in rainfall vary in response to effects such as latitude, elevation, distance from the coast, precipitation rate, condensation temperature, and relative humidity (Dansgaard, 1964). In the study area, there is a notably higher precipitation rate in the mountainous areas (385–1050 mm yr^{-1}) than in the valleys or in the coastal zone (275 mm yr^{-1}; CICESE, 2019), and average temperatures fall from 17 °C at the coast to approximately 10 °C at 1000 m a.s.l. Thus, $\delta^{18}O$ values in local surface-water decrease by -0.25‰ per 100 m elevation increase (Kretzschmar & Frommen, 2013). The analyzed inland and unmixed coastal–submarine thermal waters show no systematic shift in $\delta^{18}O$ from the GMWL and have the same stable isotopic signature as current rainfall (Figure 2f). Therefore, the thermal waters must have originally infiltrated as meteoric water at

similar climatic conditions in the geological past. This suggests that the variation of $\delta^{18}O$ and $\delta^{2}H$ values of the thermal waters mainly reflect differences in recharge elevation. A first approximation of their average recharge elevations can be deduced directly from their $\delta^{18}O$ values (Figure 7a). Thus, all the thermal waters are seen to have infiltrated at average elevations of 760–1300 m a.s.l, which are significantly higher than their discharge sites (-30–734 m a.s.l). The corresponding hydraulic-head differences (Δh) induced by the topographic relief vary within only a small range of ~570 to 790 m.

We assume that meteoric water recharges over broad areas of the mountainous landscape to the north of the ABF and that it migrates through near-surface fracture networks towards the south, where it is captured by the compartmentalized segments of the permeable fault plane. Figure 7b shows a topographic map of the study area suggesting possible locations of the meteoric recharge zones for each geothermal system along the ABF. Each location was identified based on its deduced elevation (see above) and on the assumption that it lies as close as possible to the thermal water discharge site and within the same watershed along the main river flow path. This yields distances between the recharge zones and the discharge sites (Δl) of ~8–30 km (Table S4, Electronic Appendix), which imply hydraulic-head gradients ($\Delta h/\Delta l$) of 0.02–0.09.

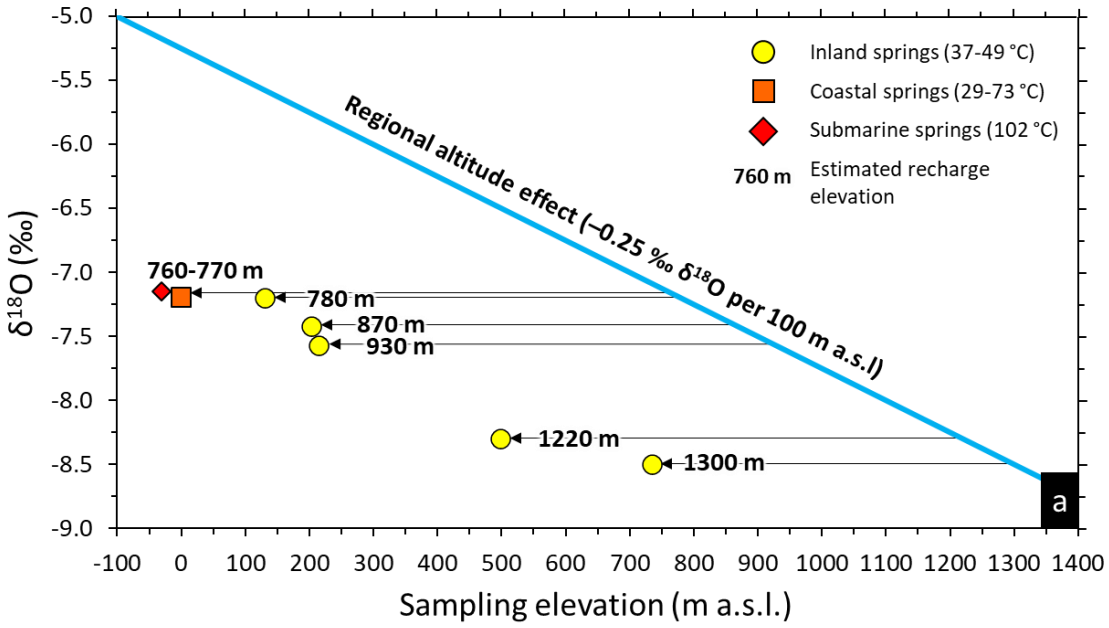

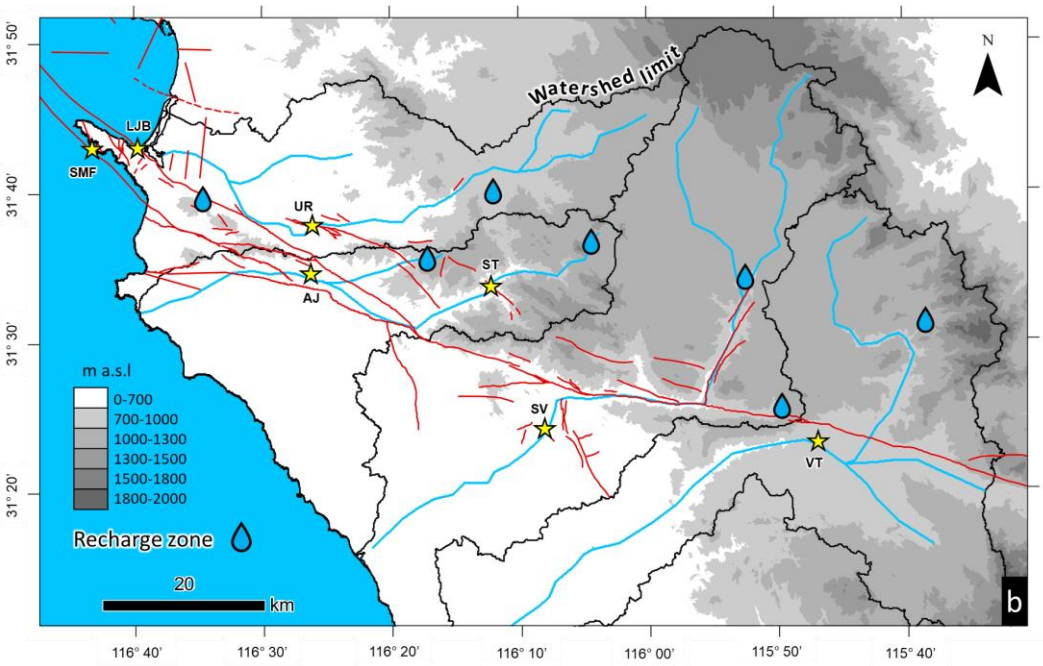

Figure 7. Meteoric water recharge of the amagmatic orogenic geothermal systems along Agua Blanca Fault. (a) Negative correlation between $\delta^{18}O$ values of thermal waters and their sampling elevation compared to that of $\delta^{18}O$ in modern surface meteoric water in northern Baja California (-0.25‰ $\delta^{18}O$ per 100 m elevation change, blue line; Kretzschmar & Frommen, 2013). The arrows give the inferred recharge elevation of each thermal water sample (see text). (b) Topographic map of the study area (after INEGI, 2022) showing the discharge locations of thermal waters (stars) and potential meteoric water recharge zones (blue drops) consistent with the estimated discharge altitudes. Also shown are perimeters of the watersheds (black lines) and rivers (blue lines) dissected by the Agua Blanca Fault. Note that two suggested recharge zones correspond to the SV site as they are at the same elevation and distance from the discharge site (SV).

4.3 Controls on the hydraulic and thermal behavior of amagmatic geothermal systems

Our study suggests that the hydraulic and thermal behavior of amagmatic orogenic geothermal systems is essentially controlled by two main parameters: the permeability of the hydraulically active fault zone and the hydraulic head gradient. Assuming that the rate of meteoric precipitation does not limit deep fluid circulation, which is a prerequisite for deep, single-pass fluid circulation (Alt-Epping et al., 2021), then these two parameters determine all key features of

the flow system. This includes the location and temperature of hot springs at the surface, the rate of water upflow, the depth of meteoric water penetration, the subsurface water residence times, and probably also the $^{3}He/He_{total}$ fractions.

The importance of permeability in controlling the flow systems is manifested by the observation that all thermal waters discharge within the highly fractured and hence permeable ABF system (Fig. 1a). In addition, all discharge sites are located at low elevations such as valley floors or along the coast (Fig. 1b), demonstrating that the hydraulic head gradient plays an important role as well, at least in controlling the location of the discharge sites. However, plotting the estimated hydraulic head gradients against the unmixed discharge temperatures does not yield a clear correlation (Fig. 8a). While hydraulic heads of 570-770 m (Figure 7) are needed to generate the thermal springs, the lack of a correlation demonstrates that the hydraulic head gradient does not directly control the upflow rates and discharge temperatures in the studied geothermal systems.

In contrast to the hydraulic head gradient, there appears to be a close link between discharge temperatures and permeability. Figure 6 shows the degree of extension along the ABF, defined as the dip-slip rate relative to the total slip rate, expressed in percent, which can be assumed to correlate positively with the permeability. The extremely high discharge temperatures ($T_{unmixed}$: 144–212 °C) observed for the Punta Banda segment located at the coast and characterized by a high degree of extension (10–15%, Figure 6) suggest the presence of highly permeable upflow zones. Moreover, together with the lack of correlation between the hydraulic head gradient and discharge temperature (Figure 8a), this implies that the permeability constitutes the first-order control of upflow rate and discharge temperature and thus on the magnitude of the resulting thermal anomaly in the surrounding rocks. Along the Punta Banda segment, permeability variations lead to an inverse relationship between hydraulic head gradients and discharge temperatures (Figure 8a), emphasizing that high discharge temperatures mainly require the presence of highly permeable upflow zones while the variation of hydraulic head gradients is less important. This is further supported by the colder inland systems ($T_{discharge}$ < 49 °C) where the degree of extension (< 10 %, Figure 6) and thus the permeability is lower. Finally, the strong control of permeability on flow rates is manifested by the existence of isolated flow compartments along the ABF system (Figure 6). Based on the variation of the recharge elevation (Figure 7) and the lack of correlation between residence time and geographic location along the ABF (Figure 6), it is evident that there are multiple isolated flow compartments as illustrated in Figure 6. The most

likely explanation for their existence is that there are low permeability zones along the ABF inhibiting connection between adjacent flow compartments.

While the hydraulic head gradient does not strongly affect upflow rates and hence discharge temperatures (Figure 8a), it has a strong control on the infiltration depth and thus the subsurface residence time as well as on the $^{3}He/^{4}He$ ratio. This is manifested by the inverse correlation between the hydraulic head gradient and both the subsurface water residence time and the $^{3}He/He_{total}$ ratio (Figures 8b,c). For hydraulically connected fault segments, theory predicts that greater penetration depths require greater horizontal lengths (Δl) between recharge and discharge sites (Tóth, 2009). For example, numerical simulations of a fault-hosted orogenic geothermal system in the Swiss Alps have shown that the length/depth ratio for single-pass flow is about 1 for realistic permeabilities (Alt-Epping et al., 2021). Therefore, the low hydraulic head gradients ($\Delta h/\Delta l$) estimated for the inland systems of the ABF (Figures 8a–c) may be reflecting deeper penetration of meteoric water. Deep circulation in the Eastern inland segment of the ABF is facilitated by the observation that the brittle–ductile transition zone lies deeper in the eastern inland segment (15–18 km deep) than in the western coastal segment (12 km deep; Figure 6). It follows that the waters may reach higher temperatures beneath the inland springs than beneath the coast. However, as the inferred fault permeability is lower in the eastern segment, Darcy's Law predicts that the rate of water upflow must be slower too. As a result, the depth at which the ascending water departs from chemical equilibrium with its wall rocks is shallower in the east than in the hot coastal zones (Figure 8e,f), thereby precluding any geothermometric signal of deeper infiltration.

The inverse relationship between discharge temperature and inferred infiltration depth (Figure 6) demonstrates that ultradeep infiltration (<< 10 km), such as is feasible in the inland systems, is not a prerequisite in amagmatic systems to achieve temperatures above 120 °C in the shallow subsurface. The only requirements are that the maximum water temperature at depth exceeds this threshold value and that the upflow rates are high. These requirements are met in the coastal zone, where meteoric water attains a maximum temperature of ~160 °C at 6 km depth (Figure 6), or shallower in the hot water plume (e.g., Wanner et al., 2019).

Previous research in the study area suggests that the helium isotope signatures reflect the ascent of mantle-derived fluids through permeable faults, combined with modification of the mantle $^{3}He/^{4}He$ ratio by mixing with radiogenic helium (Polyak et al., 1991; Barry et al., 2020). However, as mentioned above, the $^{3}He/He_{total}$ and water residence times are not only controlled by

the permeability of the fault but, more importantly, by the distance between water discharge and recharge (higher values for lower hydraulic head gradients, Figure 8c). Therefore, we suggest that longer water flow paths in the study area (i.e., deeper infiltration and hence longer residence times) allow more ^{3}He to be acquired along water flow paths. This alternative interpretation is supported by the positive correlations between $^{3}He/He_{total}$ and both the subsurface water residence time (Figure 8d) and the crustal thickness (Figure 6).

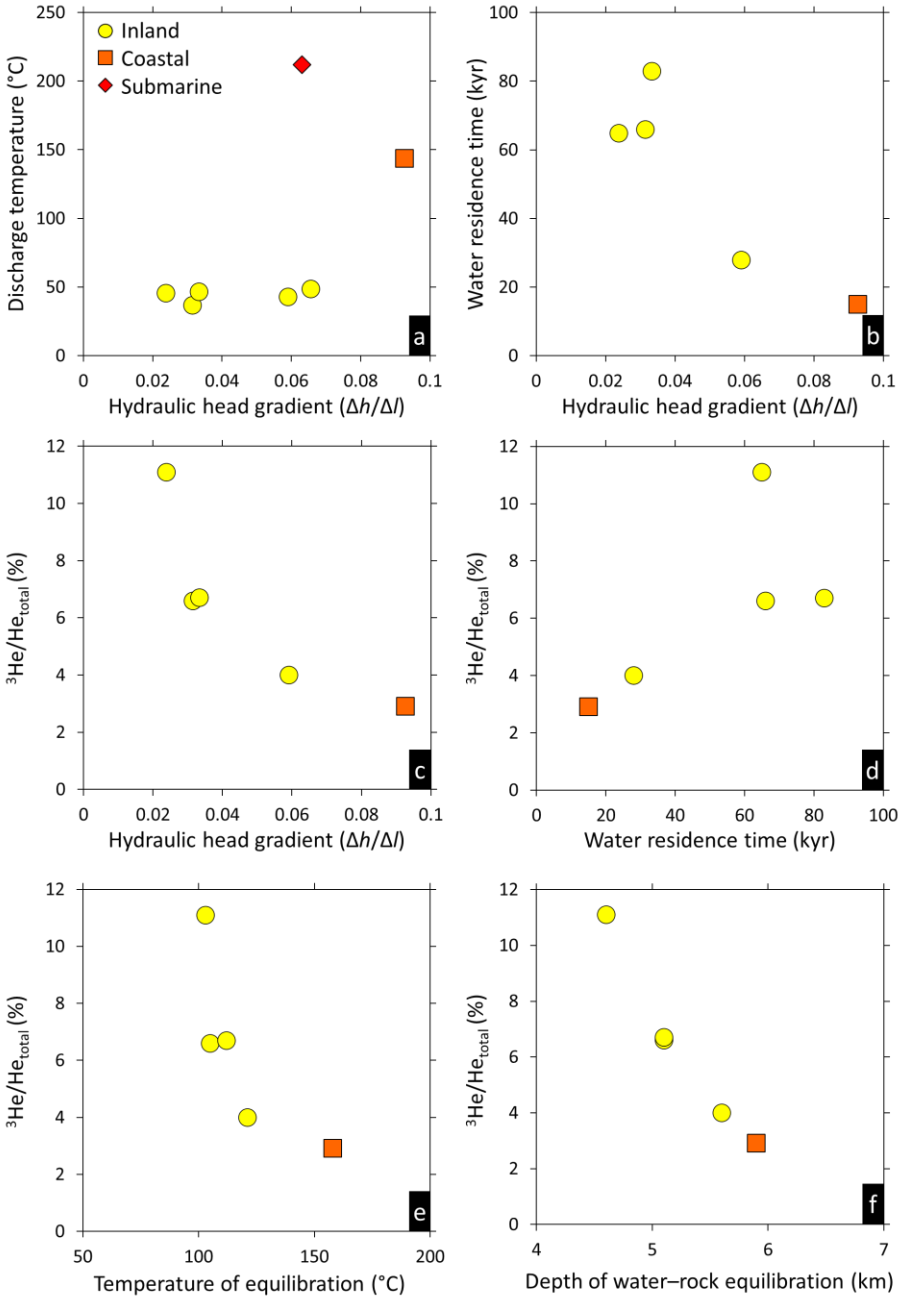

Figure 8. Correlations between proxies characterizing the flow systems of the amagmatic geothermal systems along the ABF. a) Discharge temperature vs. hydraulic head gradient, showing no mutual correlation. Note that the plotted discharge temperatures were corrected for the shallow admixture of recent seawater (Table S2 in the Electronic Appendix). b) Water residence time vs. hydraulic head gradient, showing that the hydraulic head gradient controls the residence time. c) $^{3}He/He_{total}$ vs. hydraulic head gradient, indicating that higher gradients, which correspond to shorter and shallower water flow paths, correlate with lower $^{3}He/He_{total}$ values. d) $^{3}He/He_{total}$ vs. water residence time, indicating that thermal waters with longer residence times have higher ^{3}He fractions. e) $^{3}He/He_{total}$ vs. minimum equilibration temperature, indicating that thermal waters with higher temperatures have lower ^{3}He fractions. f) $^{3}He/He_{total}$ vs. depth of water–rock equilibration, indicating that thermal waters with shallower depth of equilibration (i.e., lower upflow rates) have higher ^{3}He fractions.

5 Summary and conclusions

In this study we present geochemical, geophysical, and geological data collected along the Agua Blanca Fault, Mexico, in order to decipher the behavior of amagmatic geothermal systems. As found in other cases worldwide, our data demonstrate that these systems are driven by the infiltration of meteoric water due to the rugged regional topography. During infiltration, meteoric water increases its temperature along the local geothermal gradient while the salinity and helium concentration increase due to water–rock interaction reactions and exchange with saline porewater along the water flow path. Our diverse dataset provides strong evidence that the flow system (e.g., water upflow rates, discharge temperatures, water equilibration depth, water residence times, and $^{3}He/He_{total}$ fractions) and hence the magnitude and location of the thermal anomalies, are primarily controlled by the variability of the hydraulic head gradient and the permeability of the ABF. The hottest waters reach the surface with the fastest flow rates where the permeability reaches maximum values. In the study area, this is manifested by discharge temperatures up to 102 °C at the Pacific Ocean, where the extensional displacement of the Agua Blanca fault is highest (10–15%). On the other hand, the hydraulic head gradient controls the water flow pathways such as water residence times, water depth of infiltration and $^{3}He/He_{total}$ fractions. Our results demonstrate that, under ideal conditions (high fault permeability and hydraulic head gradients), the temperature threshold for electricity production (~120 °C) in amagmatic geothermal systems is reached at

relatively shallow depths (< 4 km), thus establishing their potential for petrothermal power production. Future exploration of orogenic geothermal systems should target valley floors intersected by active regional faults, where hydraulic head gradients and upflow rates have maximum values.

Acknowledgments

This work was supported by a CONACYT project PN-2016-01-1998 to Loïc Peiffer, and by a Swiss Government Excellence Scholarship (ESKAS) to Daniel Carbajal-Martínez, and by funds from the University of Bern, Switzerland. We are grateful to Luis Delgado (CICESE) for helping with rock sampling. We are also grateful to the Istituto Nazionale di Geofisica e Vulcanologia—Palermo (INGV-PA) for the analytical support and to Thomas Pettke (Univ. Bern) for help with LA-ICP-MS analysis.

Data Availability Statement

All the geological, geochemical and geophysical data on which this research is based are publicly available at the Zenodo repository (https://doi.org/10.5281/zenodo.7520311).

References

Allen, C. R., Silver, L. T., & Stehli, F. G. (1960). Agua Blanca fault - A major transverse structure of northern Baja California, Mexico. *Bulletin of the Geological Society of America*, *71*(4), 467–482. https://doi.org/10.1130/0016-7606(1960)71[467:ABFMTS]2.0.CO;2

Alt-Epping, P., Diamond, L. W., Wanner, C., & Hammond, G. E. (2021). Effect of Glacial/Interglacial Recharge Conditions on Flow of Meteoric Water Through Deep Orogenic Faults: Insights Into the Geothermal System at Grimsel Pass, Switzerland. *Journal of Geophysical Research: Solid Earth*, *126*(7), 1–21. https://doi.org/10.1029/2020JB021271

Alt-Epping, P., Diamond, L. W., & Wanner, C. (2022). Permeability and groundwater flow dynamics in deep-reaching orogenic faults estimated from regional-scale hydraulic simulations. *Geochemistry, Geophysics, Geosystems*. https://doi.org/10.1029/2022gc010512

Andrews, J. N., & Lee, D. J. (1979). Inert gases in groundwater from the Bunter Sandstone of England as indicators of age and palaeoclimatic trends. *Journal of Hydrology*, *41*(3–4),

233–252. https://doi.org/10.1016/0022-1694(79)90064-7

Arango-Galván, C., Prol-Ledesma, R. M., Flores-Márquez, E. L., Canet, C., & Villanueva Estrada, R. E. (2011). Shallow submarine and subaerial, low-enthalpy hydrothermal manifestations in Punta Banda, Baja California, Mexico: Geophysical and geochemical characterization. *Geothermics*, *40*(2), 102–111. https://doi.org/10.1016/j.geothermics.2011.03.002

Arnorsson, S. (1975). Application of the Silica Geothermometer in Low Temperature Hydrothermal Areas in Iceland. *Am J Sci*. https://doi.org/10.2475/ajs.275.7.763

Asta, M. P., Gimeno, M. J., Auqué, L. F., Gómez, J., Acero, P., & Lapuente, P. (2010). Secondary processes determining the pH of alkaline waters in crystalline rock systems. *Chemical Geology*, *276*(1–2), 41–52. https://doi.org/10.1016/j.chemgeo.2010.05.019

Atwater, T. (1970). Implications of Plate Tectonics for the Cenozoic Tectonic Evolution of Western North America. *Geological Society of America Bulletion*, *81*(18), 3513–3536.

Barry, P. H., Negrete-Aranda, R., Spelz, R. M., Seltzer, A. M., Bekaert, D. V., Virrueta, C., & Kulongoski, J. T. (2020). Volatile sources, sinks and pathways: A helium-carbon isotope study of Baja California fluids and gases. *Chemical Geology*, *550*(May), 119722. https://doi.org/10.1016/j.chemgeo.2020.119722

Beltrán Abaunza, J. M., & Quintanilla Montoya, A. L. (2001). Calculated heat flow for the Ensenada region, Baja California, Mexico. *Ciencias Marinas*, *27(4)*, 619--634.

Brodi, B., & Iizuka, S. (1993). Earthquake cutoff depth as a possible geothermometer-applications to central Japan. *Tectonophysics*, *225*(1–2), 63–78. https://doi.org/10.1016/0040-1951(93)90249-J

Byerlee, J. (1978). Friction of rocks. *Pure and Applied Geophysics PAGEOPH*, *116*(4–5), 615–626. https://doi.org/10.1007/BF00876528

Capasso, G., & Inguaggiato, S. (1998). A simple method for the determination of dissolved gases in natural waters. An application to thermal waters from Vulcano Island. *Applied Geochemistry*, *13*(5), 631–642. https://doi.org/10.1016/S0883-2927(97)00109-1

Carbajal-Martínez, D., Peiffer, L., Hinojosa-Corona, A., Trasviña-Castro, A., Arregui-Ojeda, S. M., Carranza-Chávez, F. J., et al. (2020). UAV-based thermal imaging and heat output estimation of a coastal geothermal resource: La Jolla beach, Baja California, Mexico. *Renewable Energy*, *168*. https://doi.org/10.1016/j.renene.2020.12.113

694 Castillo, P. R., Hawkins, J. W., Lonsdale, P. F., Hilton, D. R., Shaw, A. M., & Glascock, M. D.
695 (2002). Petrology of Alarcon Rise lavas, Gulf of California: Nascent intracontinental ocean
696 crust. *Journal of Geophysical Research: Solid Earth*, *107*(B10), ECV 5-1-ECV 5-15.
697 https://doi.org/10.1029/2001jb000666
698 CICESE. (2019). Datos climáticos diarios del CLICOM del SMN a través de su plataforma web
699 del CICESE. Retrieved from http://clicom-mex.cicese.mx/
700 Craig, H. (1961). Isotopic Variations in Meteoric Waters. *Science (New York, N.Y.)*, *133*(3465),
701 1702–3. https://doi.org/10.1126/science.133.3465.1702
702 Dansgaard, W. (1964). Stable isotopes in precipitation. *Tellus*, *16*(4), 436–468.
703 https://doi.org/10.3402/tellusa.v16i4.8993
704 Diamond, L. W., Wanner, C., & Waber, H. N. (2018). Penetration depth of meteoric water in
705 orogenic geothermal systems. *Geology*, *46*(12), 1083–1066.
706 https://doi.org/10.1130/G45394.1
707 Dragoni, M. (1993). The brittle-ductile transition in tectonic boundary zones. *Annals of*
708 *Geophysics*. https://doi.org/10.4401/ag-4282
709 Erkan, K., & Blackwell, D. (2009). Transient thermal regimes in the Sierra Nevada and Baja
710 California extinct outer arcs following the cessation of Farallon subduction. *Journal of*
711 *Geophysical Research: Solid Earth*, *114*(2), 1–18. https://doi.org/10.1029/2007JB005498
712 Fournier, R. O. (1977). Chemical geothermometers and mixing models for geothermal systems.
713 *Geothermics*, *5*(1–4), 41–50. https://doi.org/10.1016/0375-6505(77)90007-4
714 Fournier, R.O., White, D. E., & Truesdell, A. H. (1973). Geochemical indicators of subsurface
715 temperature-part 1, basic assumptions. *USGS*, *2*, 259–262.
716 Fournier, Robert O., & Potter, I. R. W. (1982). An equation correlating the solubility of quartz in
717 water from 25° to 900°C at pressures up to 10,000 bars, *46*, 1969–1973.
718 Frez, J., Acosta, J., Nava, A., Suarez, F., Gonzalez, J., Arellano, G., et al. (2004).
719 Microseismicity Studies in Northern Baja California, Mexico: the Agua Blanca Fault. AGU.
720 Retrieved from https://ui.adsabs.harvard.edu/abs/2004AGUFM.S51A0129F/abstract
721 Gastil, G., & Bertine, K. (1986). Correlation between seismicity and the distribution of thermal
722 and carbonate water in southern and Baja California, United States and Mexico. *Geology*,
723 *14*(4), 287–290. https://doi.org/10.1130/0091-7613(1986)14<287:CBSATD>2.0.CO;2
724 Gastil, R. G., Phillips, R. P., & Allison, E. C. (1975). Reconnaissance geology of the state of

Baja California. *Geological Society of America*, *140*, 201.

Giggenbach, W. F. (1988). Geothermal solute equilibria. derivation of Na-K-Mg-Ca geoindicators. *Geochimica et Cosmochimica Acta*, *52(12)*, 2749-2765.

Gold, P. O., Behr, W. M., Fletcher, J. M., Rockwell, T. K., & Figueiredo, P. M. (2020). Time-Invariant Late Quaternary Slip Rates Along the Agua Blanca Fault, Northern Baja California, Mexico. *Tectonics*, *39*(9), 1–26. https://doi.org/10.1029/2019TC005788

Grasby, S. E., & Hutcheon, I. (2001). Controls on the distribution of thermal springs in the southern Canadian Cordillera. *Canadian Journal of Earth Sciences*, *38*(3), 427–440. https://doi.org/10.1139/e00-091

Guillong, M., Meier, D. L., Allan, M. M., Heinrich, C. A., & Yardley, B. W. D. (2008). SILLS: A Matlab-Based Program for the Reduction of Laser Ablation ICP–MS Data of Homogeneous Materials and Inclusions. *Mineralogical Association of Canada Short Course*, *40*, 328–333.

Hamme, R. C., & Emerson, S. R. (2004). The solubility of neon, nitrogen and argon in distilled water and seawater. *Deep-Sea Research Part I: Oceanographic Research Papers*, *51*(11), 1517–1528. https://doi.org/10.1016/j.dsr.2004.06.009

Hilton, D. R. (1996). The helium and carbon isotope systematics of a continental geothermal system: Results from monitoring studies at Long Valley caldera (California, U.S.A.). *Chemical Geology*, *127*(4), 269–295. https://doi.org/10.1016/0009-2541(95)00134-4

INEGI. (2022). Continuo de Elevaciones Mexicano (CEM). Retrieved from https://sinegi.page.link/1av6

Inguaggiato, S., & Rizzo, A. (2004). Dissolved helium isotope ratios in ground-waters: A new technique based on gas-water re-equilibration and its application to Stromboli volcanic system. *Applied Geochemistry*, *19*(5), 665–673. https://doi.org/10.1016/j.apgeochem.2003.10.009

Junge, C. E., & Werby, R. T. (1958). The concentration of chloride, sodium, potasium, calcium, and sulfate in rain water over the United States. *Journal of Meteorology*, *15 (5)*, 417–425.

Kretzschmar, T. G., & Frommen, T. (2013). Stable Isotope Composition of Surface and Groundwater in Baja California, Mexico. *Procedia Earth and Planetary Science*, *7*, 451–454. https://doi.org/10.1016/j.proeps.2013.03.194

Kulongoski, J. T., Hilton, D. R., Cresswell, R. G., Hostetler, S., & Jacobson, G. (2008). Helium-

4 characteristics of groundwaters from Central Australia: Comparative chronology with chlorine-36 and carbon-14 dating techniques. *Journal of Hydrology*, *348*(1–2), 176–194. https://doi.org/10.1016/j.jhydrol.2007.09.048

López, D. L., & Smith, L. (1995). Fluid Flow in Fault Zones: Analysis of the Interplay of Convective Circulation and Topographically Driven Groundwater Flow. *Water Resources Research*, *31*(6), 1489–1503. https://doi.org/10.1029/95WR00422

Marine, I. W. (1979). The use of naturally occurring helium to estimate groundwater velocities for studies of geologic storage of radioactive waste. *Water Resources Research*, *15*(5), 1130–1136. https://doi.org/10.1029/WR015i005p01130

Olguín-Martínez, M. G., Peiffer, L., Dobson, P. F., Spycher, N., Inguaggiato, C., Wanner, C., et al. (2022). PyGeoT: A tool to automate mineral selection for multicomponent geothermometry. *Geothermics*, *104*(August 2021), 102467. https://doi.org/10.1016/j.geothermics.2022.102467

Ortega-Rivera, A. (2003). Geochronological constraints on the tectonic history of the Peninsular Ranges batholith of Alta and Baja California: Tectonic implications for western México. *Special Paper of the Geological Society of America*, *374*, 297–335. https://doi.org/10.1130/0-8137-2374-4.297

Ortega-Rivera, A., Suárez-Vidal, F., Mendoza-Borunda, R., & de la O, M. (2018). A multidisciplinary approach to estimate slip rate-magnitude and recurrence time for a segment of a major active fault. Case study: The Agua Blanca Fault, Valle de Agua Blanca, B.C., México. *Journal of South American Earth Sciences*, *88*(May), 1–15. https://doi.org/10.1016/j.jsames.2018.08.005

Peters, D., & Pettke, T. (2017). Evaluation of Major to Ultra Trace Element Bulk Rock Chemical Analysis of Nanoparticulate Pressed Powder Pellets by LA-ICP-MS. *Geostandards and Geoanalytical Research*, *41*(1), 5–28. https://doi.org/10.1111/ggr.12125

Van der Pluijm, B. A., & Marshak, S. (2004). *Earth structure : an introduction to structural geology and tectonics*. W.W. Norton. Retrieved from https://ben.earth.lsa.umich.edu/ES/

Polyak, B. G., Kononov, V. I., Fernandez, R., Kamenskiy, I. L., & Zinkevich, V. P. (1991). Helium isotopes in thermal fluids of baja California and adjacent areas. *International Geology Review*, *33*(12), 1218–1232. https://doi.org/10.1080/00206819109465747

RESNOM. (2017). Red Sísmica del Noroeste de México. https://doi.org/10.7914/SN/BC

Reyes, A. G., Christenson, B. W., & Faure, K. (2010). Sources of solutes and heat in low-enthalpy mineral waters and their relation to tectonic setting, New Zealand. *Journal of Volcanology and Geothermal Research*, *192*(3–4), 117–141. https://doi.org/10.1016/j.jvolgeores.2010.02.015

Rimstidt, J. D., & Barnes, H. L. (1980). The kinetics of silica-water reactions. *Geochimica et Cosmochimica Acta*, *44*(11), 1683–1699. https://doi.org/10.1016/0016-7037(80)90220-3

Rockwell, T. K., Muhs, D. R., Kennedy, G. L., Hatch, M. E., Wilson, S. M., & Klinger, R. E. (1989). Uranium-series ages, faunal correlations and tectonic deformation of marine terraces within the Agua Blanca fault zone at Punta Banda, northern Baja California, Mexico. In *Los Angeles, Society of Economic Paleontologists and Mineralogists (Pacific Section)* (pp. 1–16).

Sano, Y., & Wakita, H. (1985). Geographical distribution of He3/He4 ratios in Japan: implications for arc tectonics and incipient magmatism. *Journal of Geophysical Research*, *90*(B10), 8729–8741. https://doi.org/10.1029/JB090iB10p08729

Sano, Yuji, & Takahata, N. (2005). Measurement of noble gas solubility in seawater using a quadrupole mass spectrometer. *Journal of Oceanography*, *61*(3), 465–473. https://doi.org/10.1007/s10872-005-0055-x

Seelig, U., & Bucher, K. (2010). Halogens in water from the crystalline basement of the Gotthard rail base tunnel (central Alps). *Geochimica et Cosmochimica Acta*, *74*(9), 2581–2595. https://doi.org/10.1016/j.gca.2010.01.030

Seyfried, W. E., & Bischoff, J. L. (1979). Low temperature basalt alteration by sea water: an experimental study at 70°C and 150°C. *Geochimica et Cosmochimica Acta*, *43*(12), 1937–1947. https://doi.org/10.1016/0016-7037(79)90006-1

Smith, D. L., Nuckels, E. I., Jones, R. L., & Cook, G. A. (1979). Distribution of heat flow and radioactive heat generation in northern Mexico. *Journal of Geophysical Research*, *84*(9).

Sonney, R., & Vuataz, F. D. (2008). Properties of geothermal fluids in Switzerland: A new interactive database. *Geothermics*, *37*(5), 496–509. https://doi.org/10.1016/j.geothermics.2008.07.001

Stober, I., Zhong, J., Zhang, L., & Bucher, K. (2016). Deep hydrothermal fluid–rock interaction: the thermal springs of Da Qaidam, China. *Geofluids*, *16*(4), 711–728. https://doi.org/10.1111/gfl.12190

Stober, Ingrid., & Bucher, K. (2007). Hydraulic properties of the crystalline basement. *Hydrogeology Journal*, *15*(2), 213–224. https://doi.org/10.1007/s10040-006-0094-4

Stober, Ingrid, & Bucher, K. (1999). Origin of salinity of deep groundwater in crystalline rocks. *Terra Nova*, *11*(4), 181–185. https://doi.org/10.1046/j.1365-3121.1999.00241.x

Storey, M., Rogers, G., Saunders, A. D., & Terrell, D. J. (1989). San Quintín volcanic field, Baja California, Mexico: 'within-plate' magmatism following ridge subduction. *Terra Nova*, *1*(2), 195–202. https://doi.org/10.1111/j.1365-3121.1989.tb00352.x

Taillefer, A., Guillou-Frottier, L., Soliva, R., Magri, F., Lopez, S., Courrioux, G., et al. (2018). Topographic and Faults Control of Hydrothermal Circulation Along Dormant Faults in an Orogen. *Geochemistry, Geophysics, Geosystems*, *19*(12), 4972–4995. https://doi.org/10.1029/2018GC007965

Tian, J., Stefánsson, A., Li, Y., Li, L., Xing, L., Li, Z., et al. (2023). Geothermics Geochemistry of thermal fluids and the genesis of granite-hosted Huangshadong geothermal system , Southeast China, *109*(October 2022), 1–12. https://doi.org/10.1016/j.geothermics.2023.102647

Torgersen, T. (1980). Controls on pore-fluid concentration of 4He and 222Rn and the calculation of 4He/222Rn ages. *Journal of Geochemical Exploration*, *13*(1), 57–75. https://doi.org/10.1016/0375-6742(80)90021-7

Tóth, J. (2009). *Gravitational systems of groundwater flow: theory, evaluation, utilization*. Cambridge University Press.

Tsunogai, S. (1975). Sea salt particles transported to the land. *Tellus*, *27*(1), 51–58. https://doi.org/10.3402/tellusa.v27i1.9883

Twiss, R. J., & Moores, E. M. (1992). *Structural Geology*. Macmillan.

Vengosh, A., Heumann, K. G., Juraske, S., & Kasher, R. (1994). Boron isotope application for tracing sources of contamination in groundwater. *Environmental Science & Technology*, *28(11)*, 1968–1974.

Vidal, F. V., Welhan, J., & Vidal, V. M. (1982). Stable isotopes of helium, nitrogen and carbon in a coastal submarine hydrothermal system. *Journal of Volcanology and Geothermal Research*, *12(1–2)*, 101–110.

Vidal, V. M. V., Vidal, F. V., & Isaacs, J. D. (1981). Coastal submarine hydrothermal activity off northern Baja California: 2. Evolutionary history and isotope geochemistry. *Journal of*

Geophysical Research: Solid Earth, *86*(B10), 9451–9468. https://doi.org/10.1029/JB086iB10p09451

Waber, H. N., & Smellie, J. A. T. (2008). Characterisation of pore water in crystalline rocks. *Applied Geochemistry*, *23*(7), 1834–1861. https://doi.org/10.1016/j.apgeochem.2008.02.007

Waber, H. N., Schneeberger, R., Mäder, U. K., & Wanner, C. (2017). Constraints on Evolution and Residence time of Geothermal Water in Granitic Rocks at Grimsel (Switzerland). *Procedia Earth and Planetary Science*, *17*, 774–777. https://doi.org/10.1016/j.proeps.2017.01.026

Wanner, C., Peiffer, L., Sonnenthal, E., Spycher, N., Iovenitti, J., & Kennedy, B. M. (2014). Reactive transport modeling of the Dixie Valley geothermal area: Insights on flow and geothermometry. *Geothermics*, *51*, 130–141. https://doi.org/10.1016/j.geothermics.2013.12.003

Wanner, C., Diamond, L. W., & Alt-Epping, P. (2019). Quantification of 3-D Thermal Anomalies From Surface Observations of an Orogenic Geothermal System (Grimsel Pass, Swiss Alps). *Journal of Geophysical Research: Solid Earth*, *124*(11), 10839–10854. https://doi.org/10.1029/2019JB018335

Weiss, R. F. (1971). Solubility of Helium and Neon in Water and Seawater. *Journal of Chemical and Engineering Data*, *16*(2), 235–241. https://doi.org/10.1021/je60049a019

Wetmore, P. H., Malservisi, R., Fletcher, J. M., Alsleben, H., Wilson, J., Callihan, S., et al. (2019). Slip history and the role of the Agua Blanca fault in the tectonics of the North American-Pacific plate boundary of southern California, USA and Baja California, Mexico. *Geosphere*, *15*(1), 119–145. https://doi.org/10.1130/GES01670.1

White, D. E., Brannock, W. W., & Murata, K. J. (1956). Silica in hot-spring waters. *Geochimica et Cosmochimica Acta*, *10*(1–2), 27–59. https://doi.org/10.1016/0016-7037(56)90010-2

Williams, A. E., & Rodoni, D. P. (1997). Regional isotope effects and application to hydrologic investigations in southwestern California. *Water Resources Research*, *33*(7), 1721–1729. https://doi.org/10.1029/97WR01035

Zúñiga, W. M. T. (2010). *Mountain block recharge in the Santo Tomás valley, Baja California, México*. CICESE.